Viaggi *Progress in Earth and Planetary Science* (2018) 5:81
https://doi.org/10.1186/s40645-018-0236-z

Progress in Earth and Planetary Science

PAPER WITH FULL DATA ATTACHED Open Access

$\delta^{18}O$ and SST signal decomposition and dynamic of the Pliocene-Pleistocene climate system: new insights on orbital nonlinear behavior vs. long-term trend

Paolo Viaggi

Abstract

The global LR04 $\delta^{18}O$, the tropical ODP Site 846 sea surface temperature (SST), and the global ΔSST stack records were investigated using the advanced method for time-series decomposition singular spectrum analysis to outline the quantitative role of orbital forcings and to investigate the nonlinear dynamics of the Pliocene and Pleistocene climate system. For the first time, a detailed quantitative evaluation is provided of the $\delta^{18}O$ and SST variance paced by long-period orbital modulation, short eccentricity, obliquity, precession, and half-precession cycles. New insights into the nonlinear dynamic of the orbital components suggest considering astronomical signals as composite feedback lagged responses paced by orbitals and damped (Early Pliocene) or amplified (Mid-Late Pleistocene) in a range of − 100 to + 400% the forcing. The Early Pliocene asymptotic decay of the $\delta^{18}O$ and SST response sensitivity up to − 100% observed for the first time in all orbital responses is interpreted as damping effect of a wide global forest cover along with a possible high ocean primary productivity, through the CO_2-related negative feedbacks during time of global greenhouse. An anomalous post-Mid-Pleistocene Transition (MPT) sharply declines to near-zero in obliquity response sensitivity observed in both global $\delta^{18}O$ and tropical SST, suggesting an attenuation mechanism of the obliquity driving force and a reduction of the related feedback amplification processes. It is hypothesized the post-MPT obliquity damping has contributed to the strengthening of the short eccentricity response by mitigating the obliquity "ice killing", favoring a long-life ice sheet sensitive to a synergistic ~ 100-kyr amplification of positive feedback processes during the time of a global icy state. The global $\delta^{18}O$, the tropical SST, and the global ΔSST trend components, all explaining ~ 76% of the Plio-Pleistocene variance and significantly modifying the mean climate state, appear to be related to the long-term pCO_2 proxies, supposedly controlled by plate tectonics through the global carbon cycle (CO_2 outgassing, explosive volcanism, orography and erosion, paleogeography, oceanic paleocirculation, and ocean fertilization). Finally, singular spectrum analysis provides a valuable tool in cyclostratigraphy with the remarkable advantage of separating full-resolution time series by variance strength.

Keywords: Singular spectrum analysis, Nonlinear, Chaotic, Damping, Paleoclimate, Milankovitch, Pliocene-Pleistocene, Greenhouse

Correspondence: paolov6363@yahoo.it
Museo Geologico Giovanni Capellini, SMA, Bologna University, Via Zamboni 63, I-40126 Bologna, Italy

Introduction

The Milankovitch theory elegantly describes the collective effects of changes in the Earth's movements on its climate. Such orbital changes (eccentricity, obliquity, and precession) alter the amount and the distribution of solar radiation reaching the Earth. However, despite the studies of Kominz and Pisias (1979) and Wunsch (2004), in some textbooks or papers, there is still the misleading notion that the insolation changes are a major element controlling climate. A lot of studies have analyzed a variety of records finding the Milankovitch frequencies, but few have quantitatively investigated the hypothesis that most of the energy conveyed in paleoclimate records is not related to orbital forcing (Kominz and Pisias 1979; Raymo 1994; Wunsch 2004; Mudelsee and Raymo 2005; Hansen et al. 2013). This study applies a novel nested analytical approach based on the advanced method for signal decomposition singular spectrum analysis (SSA) with the aim of separating full-resolution time series by signal variance, the latter a useful "proxy" of the energy conveyed in paleoclimate records. SSA is a relatively new and powerful technique to processing time-series data, applicable to broad areas such as climatology, marine science, geophysics, engineering, image processing, and medicine (Vautard and Ghil 1989; Elsner and Tsonis 1996; Ghil et al. 2002; Hassani 2007). However, the SSA approach is little used in the study of paleoclimate records compared to conventional Fourier analysis, despite its capability to estimate frequencies with higher resolution than Fourier approach and to detect signal structural changes, as highlighted in the present study. Plio-Pleistocene long-term climatic cooling and the increasing glacial cycle amplitude towards the Late Pleistocene are evidence of significant changes in the climate system dynamic described in the literature, but the cause of these features remains poorly understood. The aim of this study is to investigate these topics by decomposing two selected $\delta^{18}O$ and sea surface temperature (SST) records to outline the quantitative role of astronomical forcings and the nonlinear behavior in the orbital responses and to assess the Earth's long-term controlling factors as a "stand-alone" climate system and its interaction with the astronomical one. Through the SSA, it provides for the first time a detailed quantitative evaluation of the $\delta^{18}O$ and SST signal variance in a wide spectrum of orbital components from long-period orbital modulation cycles to the half-precession, both unidentified in the previous studies of the original records. The nonlinear dynamic of the astronomical climate responses is discussed regarding new insights obtained by SSA time-series processing. A link among the atmospheric pCO_2, the sea surface temperature, and the $\delta^{18}O$ long-term trend components is also provided to support the hypothesis of a dominant non-astronomical control on the Earth's climate.

Methods/Experimental

This work contributes to the research issues by applying SSA to the global LR04 $\delta^{18}O$ stack (Lisiecki and Raymo 2005b) and the tropical Ocean Drilling Program (ODP) Site 846 SST record (Herbert et al. 2010b) (referred to as HT846 in this study), both high-resolution time series covering ~ 5 million years to capture long-term climate dynamics. The global LR04 benthic stack was obtained from 57 oceanic series globally distributed over a wide latitudinal range, including the Atlantic, Pacific, and Indian Oceans (Lisiecki and Raymo 2005a). Benthic $\delta^{18}O$ measures changes in global ice volume and deep water temperatures, which are controlled by high-latitude surface temperatures (Lisiecki and Raymo 2007). The ice volume component lags the deep water temperature signal, and the net phase of the $\delta^{18}O$ record most likely is weighted towards the slow ice volume component (Lisiecki and Raymo 2005a; Herbert et al. 2010a; Berger et al. 2016). Because the LR04 stack incorporates information from so many sites, it has a high signal-to-noise ratio and more accurately reflects changes in global climate (Lisiecki and Raymo 2005a). The original resolution of the LR04 record ranges from 1 to 5 kyr within four time intervals with constant data spacing (Lisiecki and Raymo 2005a). The average resolution is 2.5 ± 1.4 kyr. The HT846 is an alkenone-based tropical SST record located in the Eastern Equatorial Pacific (EEP). The ODP Site 846 is considered not "typical" tropical SST signal because it cools more than the ODP 662 and 722 sites, probably as the result of upwelling changes in the EEP (Herbert et al. 2010a; Lisiecki 2010b); nevertheless, its high-resolution SST record extending ~ 5 Myr makes it suitable to capture both long-term dynamics and high-frequency cycles. The original data spacing of the HT846 record is uneven throughout the 5070 kyr of the time series (Herbert et al. 2010b), with an average value of 2.3 ± 1.2 kyr. SSA requires evenly spaced records. Therefore, both records were resampled at constant time intervals of 1.0 kyr. Further details on the methodology used in this study and a discussion of the quality and reliability of the time series can be found in Additional file 1. The valuable global ΔSST stack of Martinez-Boti et al. (2015) extends 3.4 Myr with a resolution lower than that of HT846 (which is one of the ten sites included in the stack). Thus, the ΔSST stack was used in this study as a comparison record to assess some common features between the tropical Site 846 and the global SST records. The LR04 stack is orbitally tuned to an ice model driven by June 21 insolation at 65° N from La93(1,1) orbital solutions (Laskar et al. 1993), with correction of the sedimentation rate (Lisiecki and Raymo 2005a). The HT846 record is synchronized using benthic foraminiferal $\delta^{18}O$ measured in the same sediments at the study site and aligned to the LR04 stack (Herbert et al. 2010a). Unfortunately, high-resolution

extended records of CO_2 proxies to study the long-term dynamics are not currently available. The valuable simulated time series of Van de Wal et al. (2011) and Stap et al. (2016) are not suitable for the purposes of the present study because the data are not $\delta^{18}O$ independent. Nevertheless, the long-term links among climate proxies can also be studied with low-resolution records, provided that the data are temporally extended and in sufficient number and quality to ensure reliable equation fitting. In this study, the composite atmospheric boron-based pCO_2 proxy of the ODP Sites 668B-999A (Hönisch et al. 2009; Bartoli et al. 2011) and the atmospheric alkenone-based pCO_2 and SST proxies of the ODP Site 999A (Seki et al. 2010) were selected. Seki et al. (2010) proxies are rather poor in resolution but cover a long period of time. The high-resolution atmospheric CO_2 reconstructions of Martinez-Boti et al. (2015), based on multi-site boron-isotope records, were considered despite the short time series from 3.3 to 2.3 million years ago. The composite European Project for Ice Coring in Antarctica (EPICA) pCO_2 record (Luthi et al. 2008; Berger et al. 2016) and the $\delta^{13}C$-based pCO_2 proxy (Lisiecki 2010b) are also considered. In order to evaluate the trend relationships among $\delta^{18}O$, SST, and pCO_2 proxies, the high-resolution LR04 and HT846 SSA-component time series were downsampled at the approximate age of the low-resolution pCO_2 proxies from the ODP Sites 668B and 999A (Hönisch et al. 2009; Seki et al. 2010; Bartoli et al. 2011). By applying the advanced method for signal decomposition singular spectrum analysis (Vautard and Ghil 1989; Elsner and Tsonis 1996; Ghil et al. 2002; Hassani 2007), the 1.0-kyr resampled LR04 and HT846 records are partitioned in a new time series of its data components. The SSA is achieved by the computation of forward-backward covariance matrices with an order of 50 (embedding dimension) using the singular value decomposition (SVD) procedure. This method for time-series analysis can be used to isolate full-resolution independent signal components based on signal strength (variance). In contrast with Fourier analysis with fixed basis of sine and cosine functions, SSA uses an adaptive basis generated by the time series itself. As a result, the underlying model in SSA is more general and can extract amplitude-modulated wave components with higher resolution than Fourier analysis. Moreover, SSA can be effectively used as a non-parametric method for detection of structural changes in the time series, reflecting the main physical phenomena underlying the data (Vautard and Ghil 1989; Hassani 2007). In the present study, the SST and $\delta^{18}O$ SSA-components capture important aspects of the nonlinear dynamic response of the climate system in a variance-oriented way. However, some high-variance $\delta^{18}O$ and SST signal components can remain characterized by a still complex frequency spectrum with some bands dispersed in different components. A novel nested-SSA approach has been applied to these 50-order components to better separate the frequency bands and correctly estimate the variance fraction, by increasing the embedding dimension up to 300 and partitioning the component into subcomponents. More details on the SSA methodology and the complete SSA-components dataset are provided in Additional files 1 and 2. The SSA-components are then investigated by a Fourier frequency spectrum (FFS) with a data window to analyze the frequency power and to reduce spectral leakage in the Fourier spectra. The data tapering used in this study is the cs2-Hann window and the best exact N fast Fourier transform (FFT) algorithm. The peak detection uses peak-based critical limit significance levels. In this type of confidence limit, one seeks to disprove the null hypothesis where one postulates either a white noise signal or a red noise signal. The frequency peaks shown in this study are the most significant peaks above a 99.9% critical limit, unless otherwise indicated. For each peak, the time-integral squared amplitude (TISA) power is computed in relative percent. The summed power reported in the frequency analysis is merely the sum of the component powers, not the power of the composite signal that would result from the addition of the components. Because clear non-stationarity in some components complicates the Fourier representation, these signals are investigated by FFS for time intervals to capture dynamics over time. Finally, by using the La93 orbital solutions (Laskar et al. 1993) (see Additional file 1), the phase relationships to the related orbitally driven LR04-SST components were examined by cross-spectral analysis. The data were standardized on the entire Plio-Pleistocene record (mean = 0 and standard deviation = 1), and some time series were inverted in order to have the same paleoclimatic polarity (positive forcing or warming for positive standardized values). The software used in this research is AutoSignal™.

The chronostratigraphic reference charts used in this study are the ICS International Chronostratigraphic Chart (2017-02) for the Pliocene and Pleistocene and the ICS global chronostratigraphical correlation table for the last 2.7 million years (v. 2016a) for the Quaternary.

Results

Analysis of $\delta^{18}O$ SSA-components

The SSA allowed the resampled LR04 signal to be decomposed into five $\delta^{18}O$ time series, which cumulatively explain 99.5% of the original variance (LR04-filtered). The spectral framework of these $\delta^{18}O$ components (abbreviated as comp.) is diversified, with fluctuations ranging from 1330-kyr to 11-kyr periodicity (Fig. 1, Table 1). The features of the $\delta^{18}O$ components are described as follows.

$\delta^{18}O$ component-1

This component explains 81.5% of the total variance (eigenvalue 10.89) and constitutes the most significant fraction of the LR04 signal associated with a strong trend of isotopic enrichment (long-term LR04 component, LT-LR04). The FFS shows a broad spectrum of nonsignificant peaks

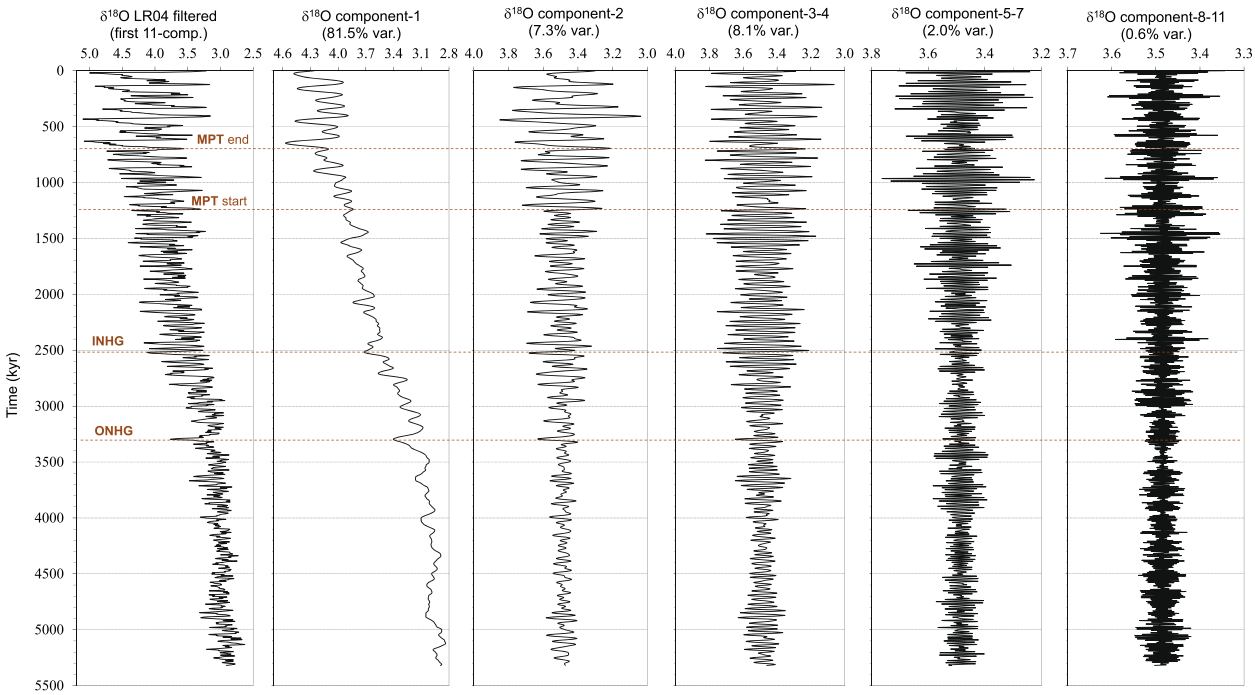

Fig. 1 Time-series panel of the five $\delta^{18}O$ components isolated from the LR04 signal by singular spectrum analysis, together with the LR04-filtered record (left) obtained by combining these data components (99.5% total variance). The *x*-axis scale (‰) is variable in relation to the variance fraction of the data components. Original LR04 $\delta^{18}O$ data from Lisiecki and Raymo (2005b) resampled at 1 kyr. Time scale in kyr

(< 50% of critical significance level) with periods equal to ~ 1.33 Myr (TISA power 77.2%), 409 kyr (10.8%), 294 kyr (6.9%), and 195 kyr (5.1%), overlapping the general trend (Fig. 1, Table 1). To separate the oscillatory terms from component-1 and estimate the variance fractions, an SSA was performed by increasing the embedding dimension to 300. Three main subcomponents (abbreviated as subcomp.) were identified equal to a reconstruction R^2 of 0.999 (Table 2).

The component-1 subcomp-1 incorporates 96.2% of the component-1 variance (81.5%), equivalent to an absolute fraction of 78.4%. It exhibits the non-Milankovitch feature of a strong isotopic trend with mild oscillations and, together with component-1, allows the subdivision of the main drift into four subtrends (Fig. 2).

These subtrends are characterized by a mild curvilinear shape caused by a terminal acceleration of the isotopic enrichment, separated by a late warming step that temporarily interrupts the drift. The first subtrend in chronological order (subtrend-I) is in the range of 5.33–3.30 Myr (Zanclean-Early Piacenzian) and culminates with a major event of isotopic enrichment at approximately 3.30 Myr, related to the first Pliocene transition of climatic deterioration known as the onset of the Northern Hemisphere Glaciation (ONHG) (Shackleton and Opdyke 1977; Blanc et al. 1983; Lourens and Hilgen 1994; Lisiecki and Raymo 2007). This subtrend is interrupted by a rapid warming at approximately 3.2 Myr, when a new isotopic drift (subtrend-II) begins and culminates at approximately 2.5 Myr (Middle Piacenzian to Gelasian) in a second major climatic event known as the intensification of the Northern Hemisphere Glaciation (INHG) (Zagwijn 1974; Lisiecki and Raymo 2007; Seki et al. 2010). Because of its global significance, this episode of climatic deterioration at 2.5 Myr was recently used to ratify the new Plio-Pleistocene limit to the base of the Gelasian (GSSP 2.58 Myr) which is formally assigned to the Pleistocene (Gibbard and Head 2009). Subtrend-III begins with warming at approximately 2.35 Myr and reaches its peak at 1.54 Myr at the end of the Santernian (Middle Gelasian-Santernian). The most recent segment of isotopic enrichment (subtrend-IV) starts with the warming at 1.45 Myr (Early Emilian) and culminates with a noticeable acceleration at 0.65 Myr, close to the beginning of the Middle Pleistocene, correlating to Marine Isotope Stage (MIS) 16. The Mid-Pleistocene Transition (MPT)—recently dated to start at approximately 1.2 Myr (Head and Gibbard 2005; Clark et al. 2006; Head et al. 2008)—which marks the beginning of the classic "Pleistocene Ice Age", falls within subtrend-IV but is not directly visible in this component. The end of the subtrend-IV marks the final stage of the MPT at about 0.7 Myr (Clark et al. 2006). After MIS-16, the cooling trend is broken by a wide swing of $\delta^{18}O$ depletion that peaks at approximately 0.40–0.30 Myr (MIS-11 and MIS-9e), referred in this study

Table 1 Main descriptive parameters and Fourier frequency results of the five $\delta^{18}O$ components isolated from the LR04 signal by singular spectrum analysis. The spectral peaks of the trend component-1 are not significant (< 50% of critical significance level) and are shown only for the purpose of discussion. Original LR04 data from Lisiecki and Raymo (2005b) are resampled at 1 kyr

$\delta^{18}O$ component rank	$\delta^{18}O$ comp. variance (%)	Frequency (kyr^{-1})	TISA power (%)	Period (kyr)	Weighted mean period (kyr)	Forcing
1	81.5	0.0007519	77.2	1330	Not significant peaks (< 50% of critical significance level)	Long-term trend + long-period orbital modulation and eccentricity cycles
		0.0024474	10.8	409		
		0.0034051	6.9	294		
		0.0051187	5.1	195		
2	7.3	0.0105636	20.9	95		Transition obliquity to short eccentricity
		0.0140889	16.8	71		
		0.0186578	22.3	54		
		0.0244330	40.1	41		
3–4	8.1	0.0244339	83.1	41	41	Obliquity
		0.0253170	12.2	39		
		0.0186593	4.7	54		
5–7	2.0	0.0422565	25.7	24	22	Precession
		0.0447325	57.6	22		
		0.0487779	16.7	21		
8–11	0.6	0.0700410	27.0	14	13	"Half-precession" (equatorial)
		0.0764743	46.5	13		
		0.0893457	26.5	11		
> 11	0.5					Noise

as the Mid-Brunhes Oscillation (MBO), containing the Mid-Brunhes Event (MBE) at approximately 0.43 Myr (Berger and Yin 2012). This subtrend pattern shows four steps of gradual buildup of the NHG, followed by a relative stasis of temperature cooling and ice growth during the last 600 kyr (MBO).

The frequency spectrum of comp-1 subcomp-1 still shows a nonsignificant residual peak at 1.33 Myr, very close to the ~ 1.2 Myr obliquity amplitude modulation cycle (Laskar et al. 2004, 2011; Boulila et al. 2011), tightly enveloped to the long-term trend, and to which the subtrend's mild terminal oscillations may be related

Table 2 Descriptive parameters and Fourier frequency results of the $\delta^{18}O$ subcomponents isolated from the LR04 component-1 by singular spectrum analysis. The processing of the subcomponents was conducted to better separate and estimate the variance fraction of specific frequency bands from still complex data components. The italicized percentage values are the absolute variance of the subcomponents (referred to the total LR04 variance)

$\delta^{18}O$ comp. rank	$\delta^{18}O$ comp. variance (%)	$\delta^{18}O$ subcomp. rank	$\delta^{18}O$ subcomp. var. (rel.) (%)	$\delta^{18}O$ subcomp. var. (abs) (%)	Frequency (kyr^{-1})	TISA power (%)	Period (kyr)		Forcing
1	81.5	1	96.2	*78.4*	0.0007519	96.6	1330	Not significant peak (< 50% of critical significance level)	Long-term trend + obliquity modulation cycle
		2	1.0	*0.8*	0.0006351	94.9	1575		Obliquity modulation cycle
					0.0024431	5.1	409		Eccentricity (long)
		3–10	2.8	*2.3*	0.0034061	16.0	294		Earth's orbit secular frequency
					0.0051192	24.5	195		Obliquity modulation cycle
					0.0061178	16.6	163		
					0.0075215	15.6	133		Eccentricity (short)
					0.0093870	12.8	107		
					0.0105656	14.5	95		

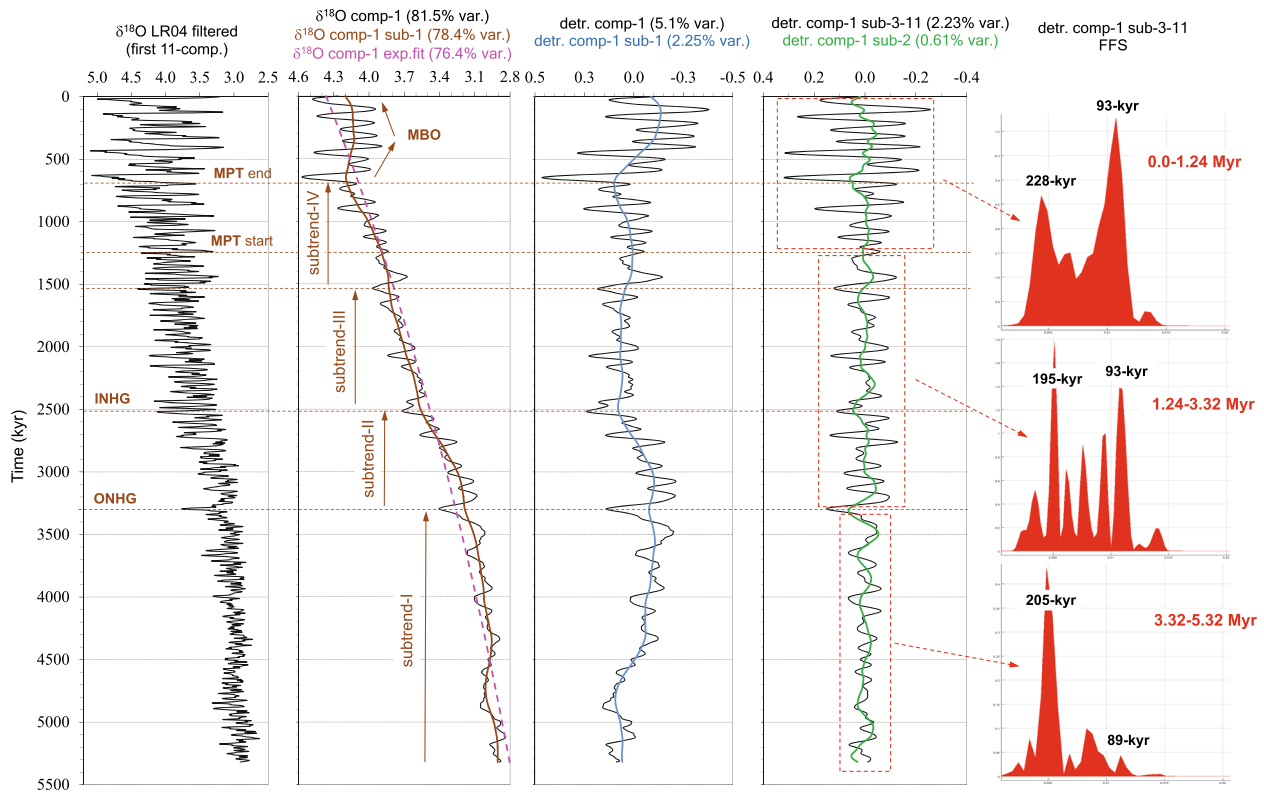

Fig. 2 Time-series panel of the $\delta^{18}O$ component-1 and its subcomponents isolated by singular spectrum analysis. $\delta^{18}O$ comp-1 exponential trend (‰) = 1.44194 + 2.92378 $e^{(-t/6963.268)}$. The vertical brown arrows show four subtrends of component-1 and their correlation to the NHG transitions known in the literature (MBO this study). To the right, the Fourier frequency spectrum of $\delta^{18}O$ detrended comp-1 subcomp-3-11 (2.23% variance) for three time intervals are highlighted by red boxes. Note the increase in amplitude after the ONHG and MPT and the power increase of the ~ 93-kyr eccentricity cycle. *x*-axis scale variable (‰). The *y*-axis scale of the frequency spectrum increases upwards. Time scale in kyr

(Fig. 2, Table 2). The comp-1 subcomp-2 contains 0.8% only of the $\delta^{18}O$ variance dominated by a 1.57-Myr periodicity (power 94.9%), which could be related to the 1.33 obliquity modulation cycle, and an ancillary term of 409 kyr. A wide spectrum of long-term cycles characterized the comp-1 subcomp-3-10, which explains 2.3% of the $\delta^{18}O$ variance (294, 195, 163, 133, 107, and 95 kyr).

To estimate the variance fraction of the "pure" long-term trend, component-1 was detrended by subtracting an exponential fitting with least squares minimization ($R^2 = 0.94$) and the oscillatory signal was processed by a 300-order SSA (Fig. 2, Table 3). The LT-LR04 exponential fit contains 93.8% of the comp-1 variance, equivalent to an absolute contribution of 76.4%, whereas the detrended oscillatory terms explain an absolute 5.1% variance. The 2% variance difference between the comp-1 subcomp-1 (78.4%) and the comp-1 exponential fit (76.4%) may be attributed to the 1.33-Myr cycle still superimposed to the comp-1 subcomp-1. Considering the variance fraction of the comp-1 subcomp-2 (0.8%, Table 2), a ~ 2.8% contribution of the 1.57–1.33-Myr cycle may be estimated. Three subcomponents were isolated from the detrended comp-1 (Table 3). The detrended comp-1 subcomp-1 explains 2.25% of the $\delta^{18}O$ variance and exhibits a spectrum dominated by a 3.75-Myr periodicity (power 95.8%) with an ancillary term of 855 kyr. Oddly, the cycle at about 1.57–1.33 Myr disappears in the detrended component-1, while a new 3.75-Myr cycle is ascribable to the 3.7-Myr g9-s9 terms of the Earth's orbit secular frequency (Laskar et al. 2011). Prevailing 409-kyr (80.6%) and 294-kyr (19.4%) cycles characterized the detrended comp-1 subcomp-2, explaining only 0.61% of the $\delta^{18}O$ variance. These periodicities may be related to the astronomically stable 405-kyr-long eccentricity cycle and to the 304-kyr Earth orbit secular frequency, respectively (Laskar et al. 2004, 2011; Boulila et al. 2011).

The detrended comp-1 subcomp-3-11 explains 2.23% of the $\delta^{18}O$ variance and shows a wide spectrum of frequency bands. A 294-kyr cycle (power 15.2%) may be related to the 304-kyr Earth orbit secular frequency. Oscillations of 163 kyr (17.2%) and 195 kyr (24.9%) may be linked to the long-period obliquity modulation cycles (~ 160–200 kyr) (Boulila et al. 2011). Finally, the short eccentricity cycles of 133 kyr (15.9%), 107 kyr (12.7%), and 95 kyr (14.1%) are also recognizable. The FFS of this subcomponent by time intervals (Fig. 2) shows two time horizons of amplitude shifting at about 3.32 Myr

Table 3 Main descriptive parameters and Fourier frequency results of the $\delta^{18}O$ subcomponents isolated from the detrended component-1 and component-2 by singular spectrum analysis. The processing of the subcomponents was conducted to better separate and estimate the variance fraction of specific frequency bands from still complex data components. The italicized percentage values are the absolute variance of the subcomponents (referred to the total LR04 variance)

$\delta^{18}O$ comp. rank	$\delta^{18}O$ comp. variance (%)	$\delta^{18}O$ subcomp. rank and var. (abs.)		$\delta^{18}O$ subcomp. var. (rel.) (%)	$\delta^{18}O$ subcomp. var. (abs) (%)	Frequency (kyr^{-1})	TISA power (%)	Period (kyr)	Forcing
1	81.5	exp.fit		93.8	*76.4*	–	–	–	Long-term trend
		detrend 6.2% (*5.1%*)	1	44.2	*2.25*	0.0002668	95.8	3748	Earth's orbit secular frequency
						0.0011701	4.2	855	Eccentricity (long)
			2	11.9	*0.61*	0.0024443	80.6	409	
						0.0034017	19.4	294	Earth's orbit secular frequency
			3–11	43.8	*2.23*	0.0034062	15.2	294	
						0.0051199	24.9	195	Obliquity modulation cycle
						0.0061180	17.2	163	
						0.0075215	15.9	133	Eccentricity (short)
						0.0093867	12.7	107	
						0.0105655	14.1	95	
2	7.3	1–4, 9–15		75.3	*5.5*	0.0105637	56.6	95	Eccentricity (short)
						0.0140872	43.4	71	
		5–8		24.4	*1.8*	0.0244321	67.5	41	Obliquity
						0.0186582	32.5	54	

(ONHG) and 1.24–0.70 Myr (MPT) that delineate three intervals, in which occur a progressive increase in signal amplitude and a relative strengthening of the short eccentricity cycle (93 kyr) at the expense of the obliquity modulation cycles (195–205 kyr), revealing a transient nonlinear behavior of this small fraction of isotopic response.

$\delta^{18}O$ component-2

Component-2 explains 7.3% of the total variance (eigenvalue 0.97) and exhibits four significant oscillatory components in the 41-kyr (power 40.1%) and 54-kyr (22.3%) obliquity bands and in the 95-kyr (20.9%) and 71-kyr (16.8%) short eccentricity bands (Fig. 3, Table 1).

Two shifting horizons of isotopic amplitude (3.32 and 1.24 Myr) are distinctly observed, correlating to the ONHG and MPT start, respectively, and defining three time intervals of increasing amplitude and a significant change in orbital periodicity. The oldest segment between 5.32 and 3.32 Myr (Zanclean-Early Piacenzian) exhibits the lowest amplitude and power and a relative prevalence of the obliquity cycle (41-kyr and 54-kyr). The eccentricity bands at 89 kyr and 102 kyr are particularly weak (Fig. 3a). From 3.32 to 1.24 Myr (Early Piacenzian-Emilian), a relative increase of the short eccentricity power (71-kyr and 91-kyr) over the obliquity cycle occurs (Fig. 3b). The most recent segment from 1.24 Myr exhibits a further increase in the average amplitude and an overwhelming power prevalence of the eccentricity 93-kyr cycle over the 41-kyr response, which maintains about the same power (Fig. 3c). To further isolate the two orbital terms from component-2, the SSA was performed by increasing the embedding dimension to 300, producing two subcomponents equal to a reconstruction R^2 of 0.998 (Fig. 3; Table 3). Subcomponent-1-4, 9-15 explains 75.3% of the component-2 variance, equivalent to an absolute variance fraction of 5.5%. It exhibits frequencies in the short eccentricity band (95-kyr, power 56.6%; 71-kyr, 43.4%). Subcomponent-5-8 explains 24.4% of the component-2 variance (1.8% absolute variance) in the obliquity frequency band (41-kyr, 67.5%, 54-kyr, 32.5%). Interestingly, the amplitude of this obliquity's subcomponent is decreasing after the MPT (Fig. 3). The change in the nonlinear dynamic of the component-2 response (transition from obliquity to short eccentricity) is configured as a sort of "switching" of the orbital power and amplitude between the 41-kyr obliquity and the 93-kyr eccentricity cycles. From this perspective, due to the change in periodicity depending on the amplitude, component-2 may be the expression of a nonlinear phase-locking mechanism between obliquity and eccentricity astronomical forcing (Tziperman et al. 2006; Ruggieri et al. 2009). Notably, by modeling the Northern Hemisphere ice volume over the last 3 Myr, Berger et al. (1999) simulated similar power spectrum changes using a combination of insolation and linearly decreasing CO_2 concentration. Imbrie et al. (2011) simulated the same spectral behavior using the Pleistocene LR04 record with a

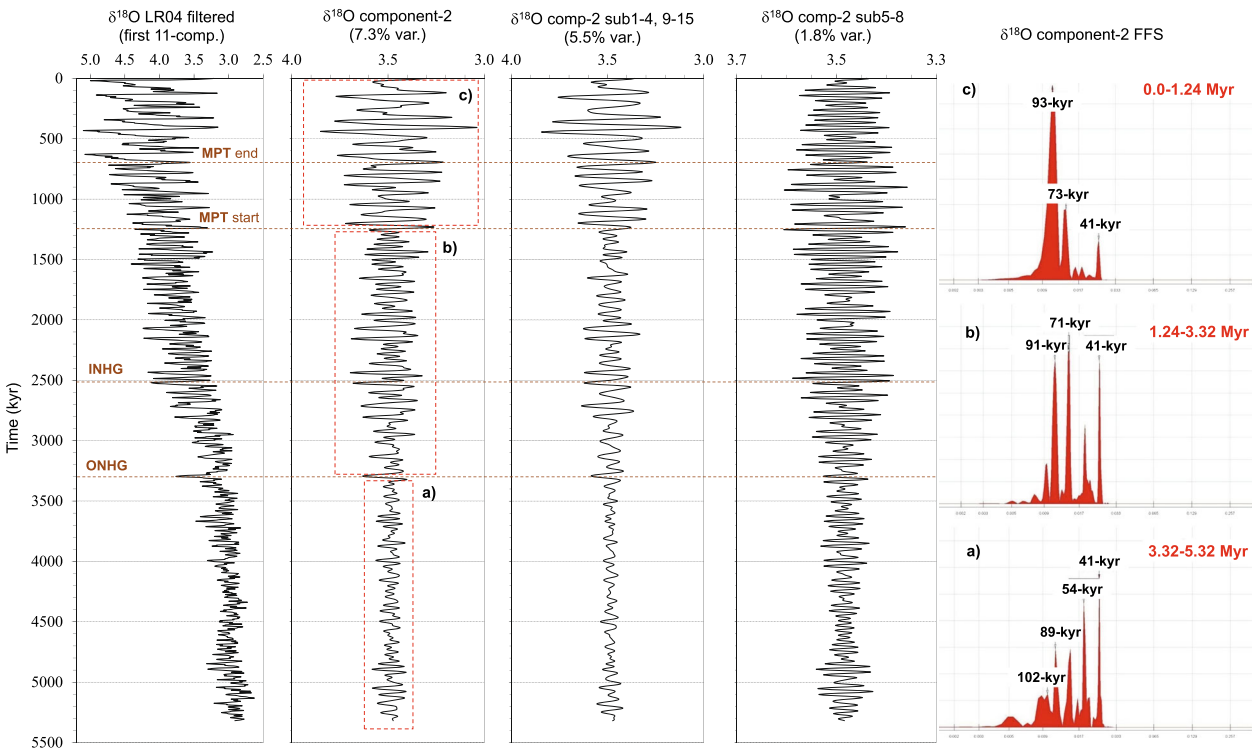

Fig. 3 Time-series panel of $\delta^{18}O$ component-2 and its subcomponents and Fourier frequency spectrum of comp-2 for three time intervals **a**, **b** and **c**, highlighted by red-labeled boxes. Note the evident increase in comp-2 amplitude after the ONHG and MPT, and the transition in periodicity from **a** obliquity to **c** eccentricity with a gradual upwards strengthening of the short eccentricity power. Interestingly, the amplitudes of the eccentricity in comp-2 subcomp-1-4, 9-15 are increasing, whereas the amplitude of the obliquity in comp-2 subcomp-5-8 is decreasing after the MPT. *x*-axis scale variable (‰). The *y*-axis scale of the frequency spectrum increases upwards. Time scale in kyr

new phase-space model of orbital forcings but with a state threshold function of the ice volume, showing that ice volume plays an important role in pacing the orbital response of the climate system. These simulated data, together with the observed features of the SSA comp-2 and detrended comp-1 subcomp-3-11 (Fig. 2), strengthen the evidence of a paleoclimatological transition where the ONHG marks the beginning of a weak and gradual sensibility of the climate system to a 93-kyr eccentricity forcing, supporting the hypothesis of an ice volume CO_2-induced control on eccentricity sensibility (Raymo 1998; Berger et al. 1999; Hansen et al. 2007; Lisiecki and Raymo 2007; Imbrie et al. 2011; Berger and Yin 2012).

$\delta^{18}O$ component-3-4

This signal explains 8.1% of the $\delta^{18}O$ variance (eigenvalue 1.08) with a 95.3% power at an obliquity-driven 41–39-kyr period (Table 1). Component-3-4 is characterized by a clear increase in the average 41-kyr amplitude and power towards the beginning of the MPT (Fig. 4a, b), followed by an amplitude stabilization and power reduction during the MPT and post-MPT (Fig. 4c). Nonstationary behavior is observed at the beginning of the MPT, where a change in the shape of the 41-kyr cycle that appears enveloped in a very weak 93-kyr signal can be noted (Fig. 4c), suggesting an apparent influence between the eccentricity and the obliquity cycles after the beginning of the MPT. The ONHG transition at 3.32 Myr does not seem to be associated with any particular features of component-3-4, except for a strong power increase in the 41-kyr cycle after the transition.

$\delta^{18}O$ component-5-7

This component explains 2.0% of the $\delta^{18}O$ variance (eigenvalue 0.27) driven by precession-related bands at ~ 22 kyr (Table 1). This precession $\delta^{18}O$ component also shows the nonlinear shape of the upwardly increasing isotopic amplitude (Fig. 1).

$\delta^{18}O$ component-8-11

Component-8-11 exhibits 0.6% of the $\delta^{18}O$ variance (eigenvalue 0.07) and contains a weight mean period at ~ 13 kyr (Table 1). Furthermore, the feature of increasing mean amplitude in this weak component is still observed (Fig. 1). From an interpretative viewpoint, component-8-11 is related to the "half-precessional" cycle of equatorial origin modulated at ~ 11 kyr (Berger et al. 2006). Hagelberg et al. (1994) found precession-related

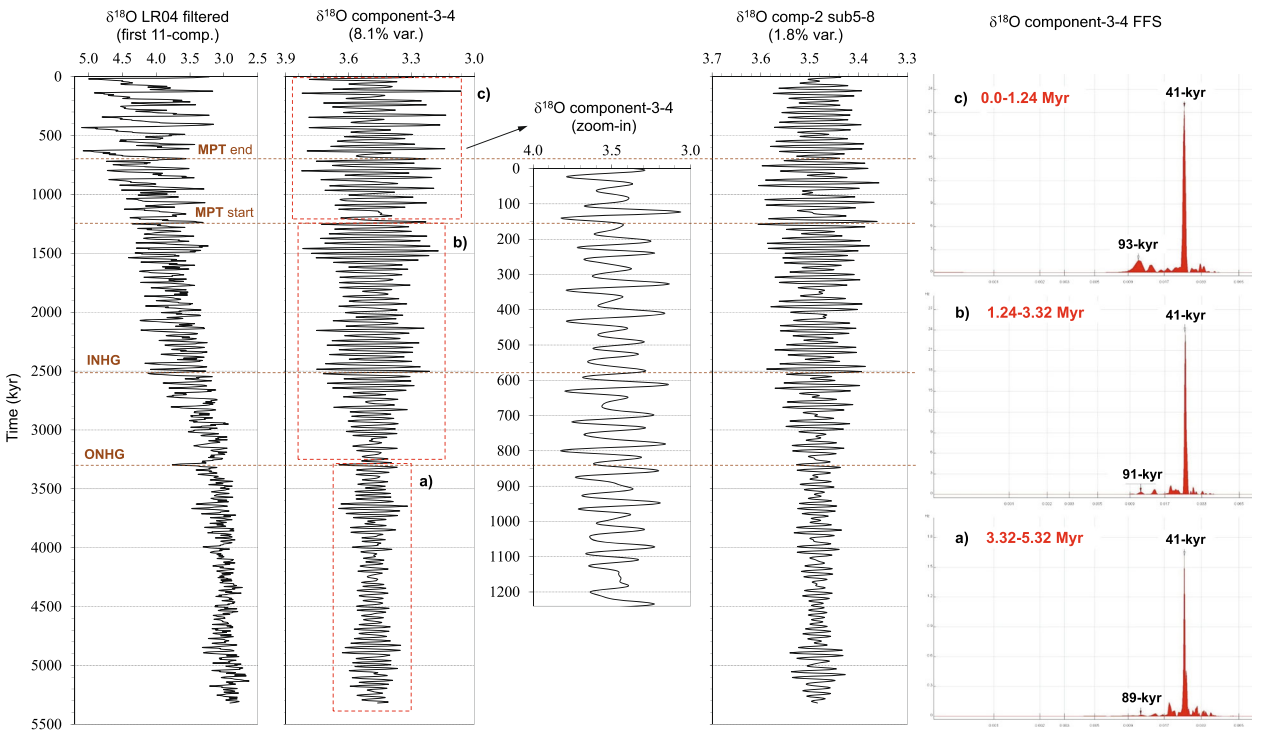

Fig. 4 Time-series panel of the $\delta^{18}O$ component-3-4 (8.1% var.) and component-2 subcomp-5-8 (1.8% var.) related to obliquity. The Fourier frequency spectrum of component-3-4 in three time intervals is highlighted by red-labeled boxes. The spectrum is always dominated by obliquity 41-kyr power. Note a clear increase in the average 41-kyr amplitude and power towards the beginning of the MPT (box 4a and 4b), followed by an amplitude stabilization and power reduction (box 4c) and an amplitude reduction (comp-2 subcomp-5-8) during the MPT and post-MPT. The envelope of two to three obliquity cycles in a weak eccentricity 93-kyr framework after the beginning of the MPT is noteworthy (box 4c and magnified time series to the right). FFS scale power increases upwards from **a** to **b** and decreases from **b** to **c**. *x*-axis scale variable (‰). Time scale in kyr

climate variability at periods from 10 to 12 kyr in three sites for the Late Pleistocene (ODP 846, ODP 663, and DSDP 609). They concluded that this variability may be derived from the high sensitivity of the tropics to summertime insolation in both hemispheres, triggering an amplified response of tropical precipitation and temperature that may be transmitted to high latitudes via Atlantic advective transport. The results of magnetic susceptibility and particle size analysis from the Northwestern Chinese Loess Plateau reveal well-defined half-precessional cycles during the last interglaciation, interpreted as a direct response to low-latitude forcing through its modulation of the East Asian summer monsoon (Sun and Huang 2006). However, despite this interesting evidence of the semi-precessional cycle of equatorial origin in the $\delta^{18}O$ deep-temperature and ice-volume signal, its contribution to the total variance of the global $\delta^{18}O$ record is less than 1%.

Analysis of the SST SSA-components

The resampled HT846 record was partitioned by SSA into five SST time series, which cumulatively explain 99.6% of the original variance (HT846-filtered) (Fig. 5, Table 4). The spectral frameworks of these SST components, ranging from 1266-kyr to 11-kyr periodicity, are very similar to that of the LR04 record. The features of the SST components are described and compared to the $\delta^{18}O$ ones as follows.

SST component-1

This component explains 87.8% of the original variance (eigenvalue 128.1) and contains the most significant fraction of the SST signal associated with a strong cooling trend (long-term HT846 component, LT-HT846). The FFS shows a broad spectrum of significant peaks with periods of ~ 1.27 Myr (TISA power 83.3%), 406 kyr (8.6%), 298 kyr (5.0%), and 193 kyr (3.1%), overlapping the general trend (Fig. 5, Table 4). A high-order SSA was performed to separate the oscillatory terms from the component-1 trend, from which three subcomponents were identified equal to a reconstruction R^2 of 0.999 (Table 5).

The component-1 subcomp-1 explains an absolute variance of 81.7% and exhibits a strong cooling trend with significant mild oscillations. The four LR04s' subtrends are generally identifiable in the tropical SST long-term components, with some differences especially in subtrend-III due to a strong cooling event at ~ 2.1 Myr (Herbert et al. 2010a), which is less evident in the $\delta^{18}O$ signal (Fig. 6). In addition, the MBO feature is

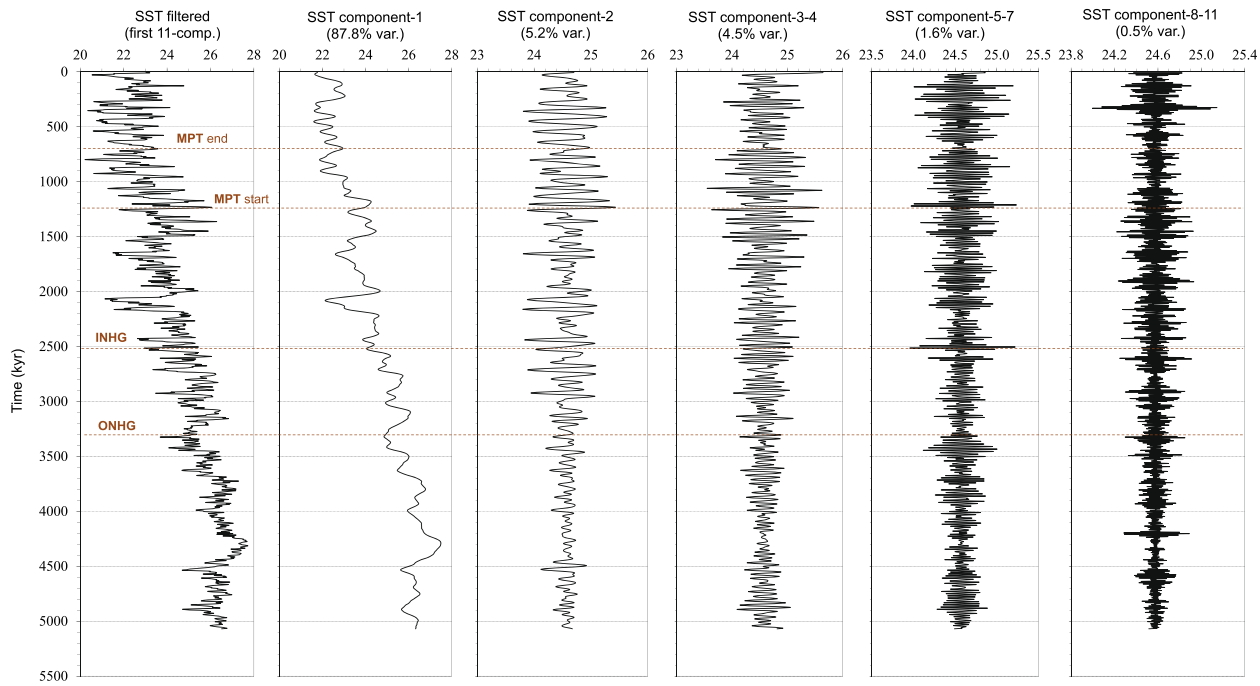

Fig. 5 Time-series panel of the five SST components isolated from the ODP Site 846 record by singular spectrum analysis with the SST-filtered record (left) obtained by combining these data components (99.6% total variance). The *x*-axis scale (°C) is variable in relation to the component's variance fraction. Original SST data from Herbert et al. (2010b) resampled at 1 kyr. Time scale in kyr

less marked in the SST signal. These differences between deep-temperature/ice-volume and sea surface temperature signals could be due to temporal effects of upwelling in the EEP "cool" region (Lisiecki 2010b).

The frequency spectrum of the SST comp-1 subcomp-1 still shows a significant peak of 1.27 Myr period (98.7% power), related to the ~ 1.2-Myr obliquity modulation cycle (Laskar et al. 2004, 2011; Boulila et al. 2011), to which the mild subtrend oscillations may be related (Table 5). The comp-1 subcomp-2 explains 3.0% of the HT846 variance dominated by a 1.50-Myr periodicity (94.1%), probably related to the same obliquity modulation cycle. A wide spectrum of long-term cycles characterized the comp-1 subcomp-3-10, explaining 3.1% of the original SST variance (399, 292, 213–193, 126, and 95 kyr).

To estimate the variance of the SST long-term trend, the component-1 was detrended by subtracting an exponential fitting with least squares minimization ($R^2 = 0.87$), and the oscillatory signal was processed by a high-order SSA (Fig. 6, Table 6). The LT-HT846 exponential fit explains 87.2% of the comp-1 variance, equivalent to an absolute contribution of 76.6%. The detrended oscillatory signal explains an absolute 11.2% variance. The 5.1% variance difference between the comp-1 subcomp-1 (81.7%) and the comp-1 exponential fit (76.6%) may be attributed to the 1.27-Myr cycle still superimposed on the comp-1 subcomp-1. Three subcomponents were isolated from the SST detrended comp-1 (reconstruction $R^2 = 0.999$). The detrended comp-1 subcomp-1 explains 5.56% of the SST original variance and exhibits a spectrum dominated by 1.37-Myr (power 51.9%) and 3.6-Myr (40.6%) cycles, with an ancillary term of 827 kyr. Again, the 3.7- to 3.6-Myr cycle appears in the LR04 and HT846 detrended comp-1 subcomp-1 only; however, in the HT846 record, the 1.37-Myr cycle does not disappear. Therefore, the 5.56% tropical SST variance (detrended comp-1 subcomp-1) related to the long-term cycles (1.37-Myr obliquity modulation cycle and 3.6-Myr Earth orbit secular frequency) is consistent with the 5.1% variance estimate by difference from comp-1 subcomp-1 (which includes the 1.27-Myr cycle only).

Prevailing 405-kyr (70.3%) and 300-kyr (29.7%) cycles characterize the detrended comp-1 subcomp-2 explaining 2.81% of the SST variance. These frequencies may be related to the astronomically stable 405-kyr-long eccentricity cycle and to the 304-kyr Earth orbit secular frequency (Laskar et al. 2004, 2011; Boulila et al. 2011). The detrended comp-1 subcomp-3-11 explains 2.84% of the SST variance and shows a wide spectrum of frequency bands. A 295-kyr cycle (power 15.4%) can be attributed to the 304-kyr Earth orbit secular frequency. Oscillations of 193 kyr (45%) and 148 kyr (6.7%) may be linked to the long-period obliquity modulation cycles (~ 160–200 kyr) (Boulila et al. 2011). Finally, weak short eccentricity cycles of 136 kyr (9.2%), 126 kyr (14%), and 95 kyr (9.7%) are also recognizable. The FFS of this subcomponent by time intervals (Fig. 6) shows a relative strengthening of the short

Table 4 Main descriptive parameters and Fourier frequency results of the five ODP Site 846 SST components isolated by singular spectrum analysis. Original SST data from Herbert et al. (2010b) resampled at 1 kyr

SST component rank	SST comp. variance (%)	Frequency (kyr^{-1})	TISA power (%)	Period (kyr)	Weighted mean period (kyr)	Forcing
1	87.8	0.0007899	83.3	1266		Long-term trend + long-period orbital modulation and eccentricity cycles
		0.0024651	8.6	406		
		0.0033527	5.0	298		
		0.0051684	3.1	193		
2	5.2	0.0105090	32.6	95		Transition obliquity to short eccentricity
		0.0110927	26.3	90		
		0.0144249	41.1	69		
		0.0244798	–	41	Very low power peak	
3–4	4.5	0.0244852	69.3	41	40	Obliquity
		0.0252735	18.4	40		
		0.0268223	12.3	37		
5–7	1.6	0.0439726	31.6	23	22	Precession
		0.0463271	43.1	22		
		0.0487111	25.3	21		
8–11	0.5	0.0732060	36.7	14	12	"Half-precession" (equatorial)
		0.0767562	30.5	13		
		0.0946970	32.8	11		
> 11	0.4					Noise

eccentricity cycle (93-kyr) at the expense of the obliquity modulation cycles (~ 195- to 158-kyr), whereas the increase in signal amplitude by time is not observable post-MPT.

SST component-2

This component explains 5.2% of the total variance (eigenvalue 7.56) and exhibits a basically 95- to 90-kyr short eccentricity periodicity (58.9%) with a 69-kyr term (41.1%) and a very weak but significant 41-kyr obliquity oscillation (Fig. 7; Table 4). Compared to the $\delta^{18}O$ comp-2, the two shifting horizons of increasing amplitude (ONHG and MPT start) and the change in orbital periodicity from 41–54 to ~ 93 kyr by three time segments are less evident (Fig. 7a–c). The transition from obliquity to short eccentricity is less evident but still present as shown also by the subcomponent analysis (Table 6). Three subcomponents were isolated by

Table 5 Descriptive parameters and Fourier frequency results of the ODP Site 846 SST subcomponents isolated from the SST component-1 by singular spectrum analysis. The processing of the subcomponents was done to better separate and estimate the variance fraction of specific frequency bands from still complex data components. The italicized percentage values are the absolute variance of the subcomponents (referred to the total SST variance)

SST comp. rank	SST comp. variance (%)	SST subcomp. rank	SST subcomp. var. (rel.) (%)	SST subcomp. var. (abs) (%)	Frequency (kyr^{-1})	TISA power (%)	Period (kyr)	Forcing
1	87.8	1	93.0	*81.7*	0.0007899	98.7	1266	Long-term trend + obliquity modulation cycle
		2	3.4	*3.0*	0.0006678	94.1	1497	Obliquity modulation cycle
					0.0024657	5.9	406	Eccentricity (long)
		3–10	3.5	*3.1*	0.0025065	8.2	399	
					0.0034190	18.5	292	Earth's orbit secular frequency
					0.0046896	15.3	213	Obliquity modulation cycle
					0.0051832	36.9	193	
					0.0079507	12.7	126	Eccentricity (short)
					0.0105043	8.4	95	

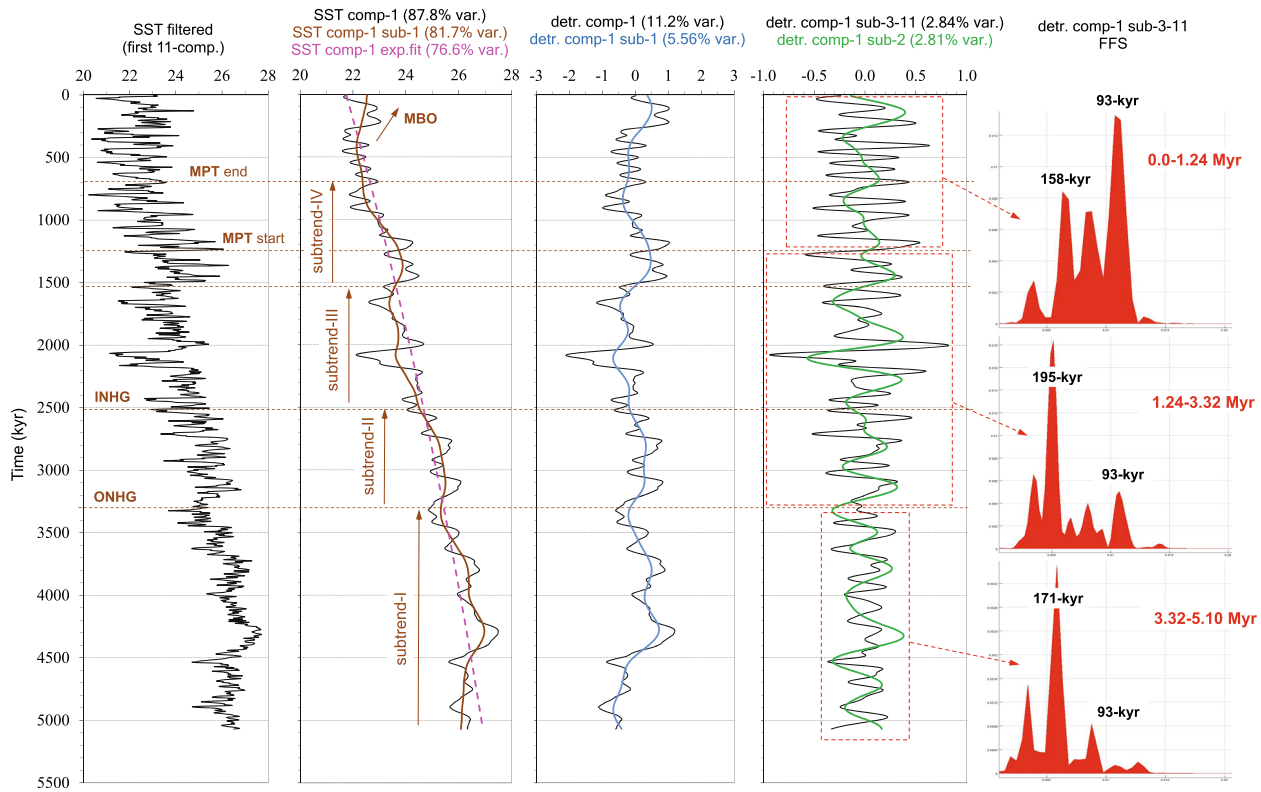

Fig. 6 Time-series panel of the ODP Site 846 SST component-1 and its subcomponents isolated by singular spectrum analysis. SST comp-1 exponential trend (°C) = 33.58041–11.84075 $e^{(-t/8830.503)}$. The vertical brown arrows show four subtrends of component-1 and their correlation to the NHG transitions known in the literature (MBO this study). To the right, Fourier frequency spectrum of SST detrended comp-1 subcomp-3-11 (2.84% variance) for three time intervals are highlighted by red boxes. Note the increase in amplitude after the ONHG (but not after the MPT) and the power increase of the ~ 93-kyr eccentricity cycle. *x*-axis scale variable (°C). The *y*-axis scale of the frequency spectrum increases upwards. Time scale in kyr

a high-order SSA ($R^2 = 0.999$). Subcomponent-1-4 explains 3.65% of the original SST variance and shows a frequency spectrum in the short eccentricity band (95-kyr, power 43.2% and 69-kyr, 56.8%). Subcomponent-5-8, 11-15 explains 1.27% variance in a still complex transition spectrum from the obliquity (53-kyr, 60.2%) to eccentricity band (126-kyr, 39.8%). Finally, subcomp-9-10 explains only 0.27% of the SST variance in the obliquity frequency band (45-kyr, 62.2%; 41-kyr, 37.8%).

SST component-3-4

This component explains 4.5% of the SST variance (eigenvalue 6.56) at the 87.7% obliquity-driven 41–40-kyr period (Table 4). The SST component-3-4 is still characterized by a less evident increase in the average amplitude by time approaching the beginning of the MPT (Fig. 8a, b), followed by a clear decrease in amplitude after the MPT start (Fig. 8c). A slight change in the shape of the 41-kyr cycle that appears enveloped in a very weak ~ 93-kyr signal can be observed after 1.2 Myr (Fig. 8c).

SST component-5-7

This component explains 1.6% of the SST variance (eigenvalue 2.24) driven by precession frequency bands at ~ 22 kyr (Table 4), similar to the precession $\delta^{18}O$ component.

SST component-8-11

Component-8-11 explains a total 0.5% of the SST variance (eigenvalue 0.74) and shows a weight mean period at ~ 12 kyr (Table 4). An increasing mean amplitude in this weak component is still observed (Fig. 5). This component is similar to that of the $\delta^{18}O$ identified in this study and can be related to the "half-precessional" cycle of equatorial origin modulated at ~ 11 kyr (Berger et al. 2006).

Summary of $\delta^{18}O$ and SST forcing variance contribution

The SSA results allow the LR04 $\delta^{18}O$ and ODP Site 846 SST forcing variance contribution to be estimated quantitatively in detail. A complex envelope of long-term orbital cycles accounts for a maximum of 5.1% of the $\delta^{18}O$ variance (due to a small fraction of short eccentricity in detrend

Table 6 Main descriptive parameters and Fourier frequency results of the ODP Site 846 SST subcomponents isolated from the detrended comp-1 and comp-2 by singular spectrum analysis. The processing of the subcomponents was made in order to better separate and estimate the variance fraction of specific frequency bands from still complex data components. The italicized percentage numbers are the absolute variance of the subcomponents (referred to the total SST variance)

SST comp. rank	SST comp. variance (%)	SST subcomp. rank and var. (abs.)		SST subcomp var. (rel.) (%)	SST subcomp var. (abs) (%)	Frequency (kyr^{-1})	TISA power (%)	Period (kyr)	Forcing
1	87.8	exp.fit		87.2	*76.6*	–	–	–	Long-term trend
		detrend 12.8% (*11.2%*)	1	49.6	*5.56*	0.0002758	40.6	3626	Earth's orbit secular frequency
						0.0007313	51.9	1367	Obliquity modulation cycle
						0.0012092	7.5	827	Eccentricity (long)
			2	25.1	*2.81*	0.0024667	70.3	405	
						0.0033343	29.7	300	Earth's orbit secular frequency
			3–11	25.4	*2.84*	0.0033896	15.4	295	
						0.0051716	45.0	193	Obliquity modulation cycle
						0.0067394	6.7	148	
						0.0073694	9.2	136	Eccentricity (short)
						0.0079678	14.0	126	
						0.0104995	9.7	95	
2	5.2	1–4		70.2	*3.65*	0.0105084	43.2	95	Eccentricity (short)
						0.0144299	56.8	69	
		5–8, 11–15		24.5	*1.27*	0.0079524	39.8	126	Transition obliquity to short eccentricity
						0.0187962	60.2	53	
		9–10		5.2	*0.27*	0.0220179	62.2	45	Obliquity
						0.0244820	37.8	41	

comp-1 subcomp-3-11; Table 3). Within the 2.23% variance of the $\delta^{18}O$ detrend comp-1 subcomp-3-11, a ~ 0.95% short eccentricity contribution may be roughly estimated by using the TISA power of the short eccentricity terms (42.7% of 2.23% variance). This approach is justified because of the low variance of the detrend comp-1 subcomp-3-11, causing a negligible error. Therefore, $\delta^{18}O$ long-period orbital modulation cycles (1.57–1.33 Myr and ~ 160–200 kyr obliquity amplitude modulation; 3.75 Myr and ~ 300 kyr Earth orbit secular frequencies) and the ~ 405-kyr-long eccentricity cycles tightly overlapped to the $\delta^{18}O$ trend, influencing the Earth's climate with an estimated variance of ~ 4.2%. Regarding the tropical SST, a similar complex envelope of long-term orbital cycles account for a maximum 11.2% of the HT846 variance (Table 6), and by subtracting the small variance of the short eccentricity term (32.9% of 2.84%, variance = 0.93%), a contribution of ~ 10.3% can be estimated.

Long-term cycles (1.5–1.0 Myr) were previously observed in the planktonic $\delta^{18}O$ record of ODP Site 625B from the Gulf of Mexico and interpreted as a low-frequency component of the climate system, likely unrelated to orbital forcing (Joyce et al. 1990). Instead, according to Lourens and Hilgen (1994), the long-term 1.3-Myr period observed from some Mediterranean and equatorial Atlantic and Pacific sites resulted from a long-term obliquity modulation cycle. Through a correlation between Cenozoic icehouse sequences and astronomical cycles, Boulila et al. (2011) demonstrate a close correlation between ~ 1.2-Myr obliquity modulation cycles and third-order eustatic sequences, suggesting glacioeustasy as the major driving process of third-order sequences in an icehouse world. A complex envelope of Plio-Pleistocene long-term astronomical cycles and especially the 1.57–1.33-Myr obliquity amplitude modulation to which the mild NHG's subtrend terminal oscillations may be related by transient interaction on the long-term trend are further geological evidences of the chaotic behavior of the Solar System (Laskar et al. 2004, 2011; Boulila et al. 2011; Westerhold et al. 2017), and the SSA results show that their influence on Earth's climate, estimated for the first time in this study, have important differences in variance (global $\delta^{18}O$ ~ 4.2%; tropical SST ~ 10.3%). Interestingly, the tight overlap of these long cycles could be the reflection of a close link between these weak orbital forcings and the much more effective forcing at the origin of the long-term trends through a temperature-ice volume-induced control on the long-cycle sensibility. The lack of the ~ 1.2-Myr eustatic cycles in the Mesozoic greenhouse world (ephemeral or no ice sheets) (Boulila et al. 2011) may support this hypothesis.

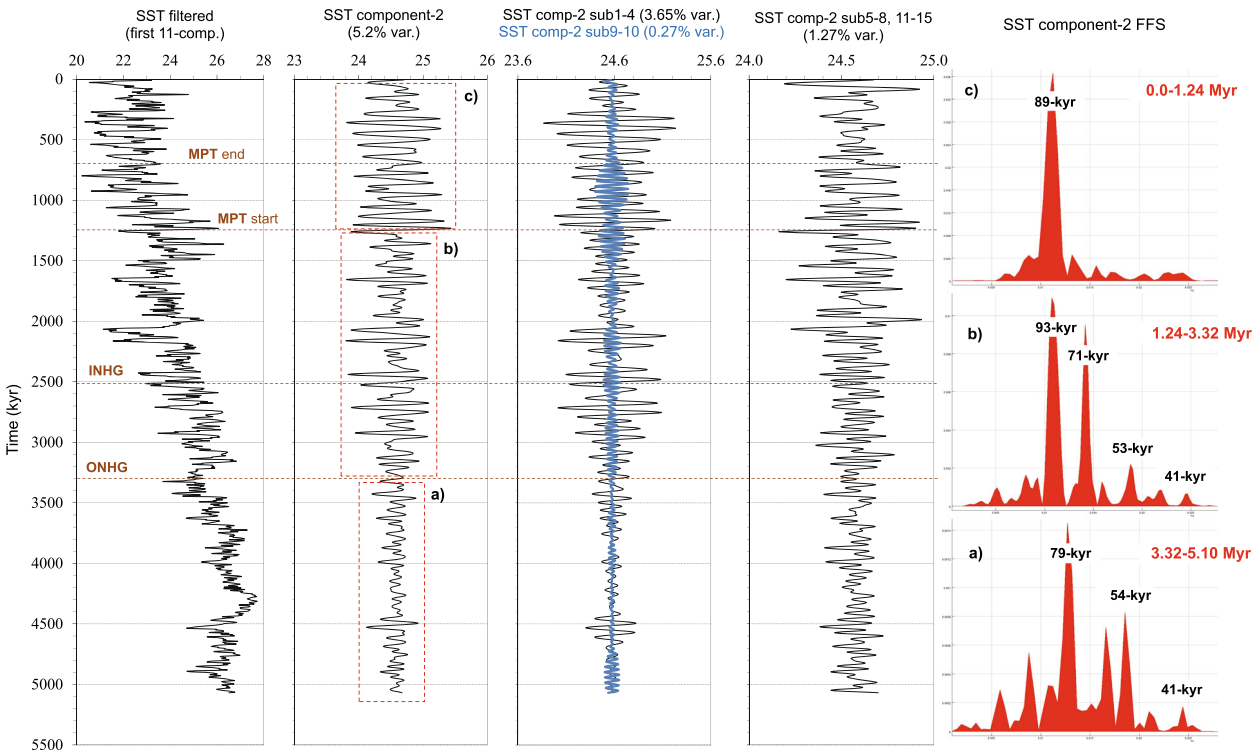

Fig. 7 Time-series panel of ODP Site 846 SST component-2 and its subcomponents and Fourier frequency spectrum of comp-2 for three time intervals **a**, **b** and **c**, highlighted by red-labeled boxes. The transition nature from **a** obliquity to **c** short eccentricity is less evident in this tropical SST site, but still present. The increasing amplitude of the short eccentricity is more clear in subcomp-1-4. The obliquity decrease after the MPT is still shown by subcomp-9-10. *x*-axis scale variable (°C). The *y*-axis scale of the frequency spectrum increases upwards. Time scale in kyr

The short eccentricity does not manifest itself as a "pure" $\delta^{18}O$ component; rather, it appears to move gradually to the Pleistocene climate signal as an interaction subcomponent only, with a long-term response (detrend comp-1 subcomp-3-11, ~0.95% variance) and the obliquity-eccentricity transitional component-2 (component-2 subcomp-1-4, 9-15, 5.5% variance). Therefore, the short eccentricity cycle contributes ~6.5% to the global Plio-Pleistocene $\delta^{18}O$ signal. Similarly, the SST detrend comp-1 subcomp-3-11 explains ~0.93% of short eccentricity variance, and a 3.65% fraction is recorded in the SST comp-2 subcomp-1-4. A small fraction of short eccentricity terms are still recorded in the SST comp-2 subcomp-5-8, 11-15 for which a 0.5% variance can be estimated (39.8% of 1.27% variance), resulting in a SST short eccentricity total variance of ~5.1%. These values agree with the consideration that the amount of insolation perturbation at the eccentricity-driven ~100-kyr period is too small to directly cause climate change of an ice age amplitude (Imbrie et al. 1993; Berger et al. 1999, 2006; Lisiecki 2010a).

The 41-kyr obliquity cycle appears to transfer to the climate system both as a "pure" $\delta^{18}O$ component, with signal strength of 8.1% (component-3-4), and as an interaction subcomponent like the obliquity-eccentricity transitional component-2 (comp-2 subcomp-5-8, 1.8% var.). Therefore, the total $\delta^{18}O$ signal variance in the 41-kyr obliquity band is estimated to be 9.9%. The SST shows a similar behavior characterized by a "pure" component-3-4 (4.5% variance) plus transitional obliquity-eccentricity subcomponents (comp-2 subcomp-9-10, 0.27% var.; comp-2 subcomp-5-8, 11–15, ~0.76%), from which a total obliquity contribution of 5.5% may be estimated.

The precession and semi-precession $\delta^{18}O$ variance can be evaluated at about 2.0% and 0.6%, close to the SST contribution of 1.6% and 0.5%, respectively. In summary, the variance of the $\delta^{18}O$ orbital components related to long-term, short eccentricity, obliquity, precession, and semi-precession cycles can be evaluated at approximately 4.2%, 6.5%, 9.9%, 2.0%, and 0.6%, respectively (total 23.2% variance), whereas the orbital SST components account for 10.3%, 5.1%, 5.5%, 1.6%, and 0.5%, respectively (total 23.0% variance). Within orbital forcings, the impact of the obliquity cycle appears to be the most consistent in the LR04 stack. In the tropical HT846 record, the most consistent orbital signal is related to the long-term cycles. These results agree with those of Kominz and Pisias (1979), which state that the fraction of the record variance related to orbital changes is less

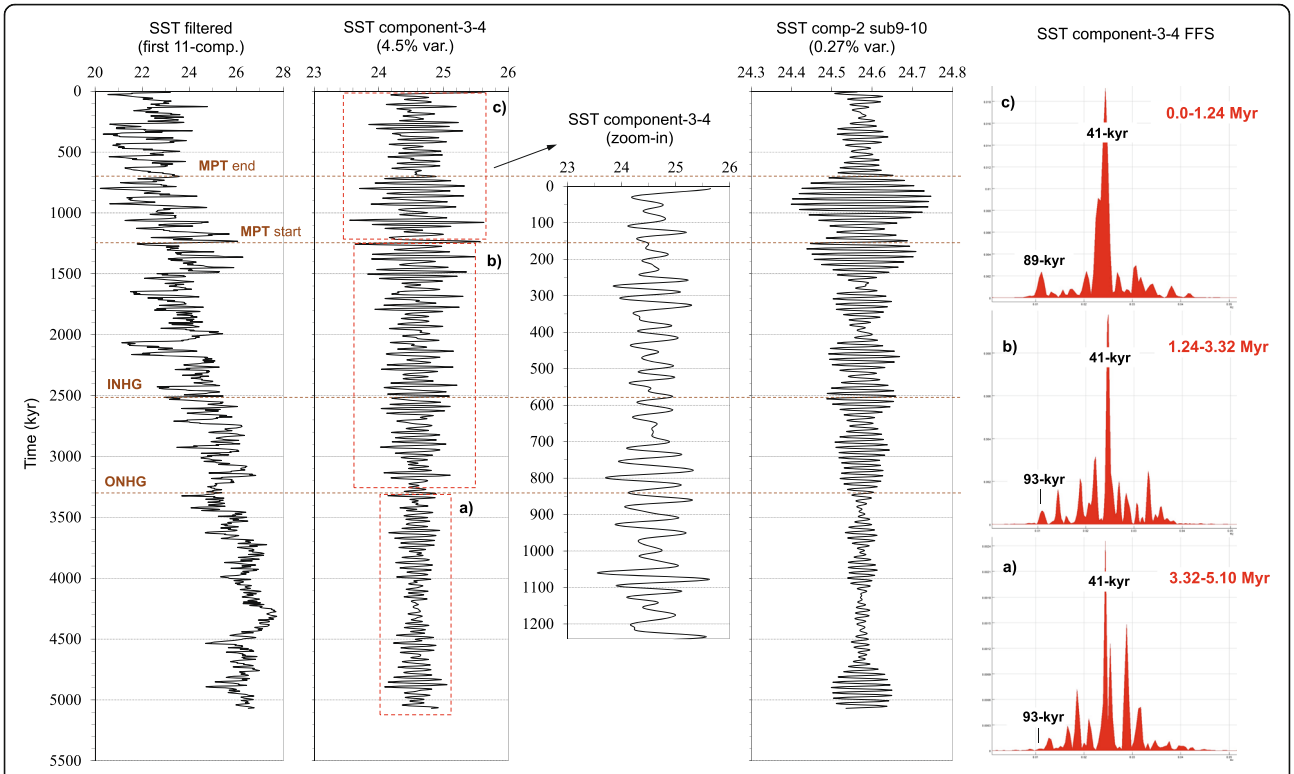

Fig. 8 Time-series panel of the ODP Site 846 SST obliquity's component-3-4 (4.5% var.) and component-2 subcomp-9-10 (0.27% var.). Fourier frequency spectrum of comp-3-4 by three time intervals highlighted by red labeled boxes. The spectrum is always dominated by obliquity 41-kyr power. Note a clear increase in the average 41-kyr amplitude and power towards the beginning of the MPT (box 8a and 8b), followed by a clear decrease in amplitude after the beginning of the MPT (box 8c and comp-2 subcomp-9-10). The envelope of two to three obliquity cycles in a weak eccentricity ~ 93-kyr framework after the beginning of the MPT is less evident (box 8c and magnified time series to the right). FFS scale power increasing from **a** to **b** and was constant from **b** to **c**. *x*-axis scale variable (°C). Timescale in kyr

than 25%, and of Wunsch (2004), which states that this fraction never exceeds 20%. Interestingly, the cumulative influence on the Earth's climate of orbital forcings estimated from the global $\delta^{18}O$ stack is equal to that of the tropical SST single record, while the individual contribution of each astronomical term is quite different. This result could be attributed to the latitudinal gradients of orbital forcings (Berger 1978; Liu and Herbert 2004), while the constancy of the long-term variance might reflect a global latitude-independent nature of the paleoclimatic trend's control factors. The fact that the $\delta^{18}O$ and SST orbital components explain ~ 23% of the total variance clearly shows that astronomical forcing does not play a major role in guiding the response of the climate system in the Plio-Pleistocene, in agreement with Kominz and Pisias (1979), Raymo (1994), Wunsch (2004), and Mudelsee and Raymo (2005). However, ~ 76% of the Plio-Pleistocene climate variance is related to non-Milankovitch long-term controlling factors, drives approximately three fourths of the energy conveyed in paleoclimate records, and thus constitutes the main Earth's climate system. This robust and stable trend signal needs to be explained.

Statistical analysis of the mean climate state through time

The SSA time series allow a quantitative analysis of the mean climate state through time. The Plio-Pleistocene $\delta^{18}O$ and SST components and the solution of orbital forcings (Laskar et al. 1993) were standardized (mean = 0, standard deviation = 1) and binned at three arbitrary constant time intervals (532 kyr, 760 kyr, and 1064 kyr) to avoid data density distortion in descriptive statistics and significance tests of mean differences among groups (Table 7). Some data were inverted in order to have the same paleoclimatic polarity (Fig. 9).

As observed in the comparison of the 95% confidence interval (CI) for the means (Fig. 9a, c) and in the significance tests of the mean differences in the analysis of variance (ANOVA) table (Table 7), the $\delta^{18}O$ and SST trend components (comp-1, comp-1 subcomp-1, and comp-1 exponential fit) can very significantly change the signal mean for different time intervals. Instead, the $\delta^{18}O$ and SST orbital components (comp-2-11) and the astronomical forcings modified the mean with little significance or no significance. These results are similar across all three binned time intervals showing that this feature is not a time frame artifact (Table 7). In more

detail, the mean reaches a deviation from the standardized mean up to − 1.51–1.18 standard units through the time segments in the $\delta^{18}O$ component-1, up to − 1.50–1.21 in the $\delta^{18}O$ comp-1 subcomp-1, and in the range − 1.72–1.40 in the $\delta^{18}O$ comp-1 exponential fit. The SST trend components exhibit similar results with deviations up to − 1.45–1.27, − 1.49–1.33, and − 1.67–1.50 for the comp-1, comp-1 subcomp-1, and comp-1 exponential fit, respectively. The $\delta^{18}O$ and SST orbital signals reach maximum values of − 0.08–0.09 and − 0.09–0.04 standard deviations, respectively. Eccentricity reaches a maximum deviation from the standardized mean of − 0.30–0.28 units. Obliquity ranges from − 0.12 to 0.12 and precession from − 0.02 to 0.01. The insolation mean (65° N at June 21) oscillates in the range of − 0.08–0.06. The ANOVA analysis was also done to all single orbital components, obtaining similar results. The histograms of the Plio-Pleistocene $\delta^{18}O$ and SST astronomical components-2-11, compared to that of the trend component-1 subcomp-1 (Fig. 9b, d), show a roughly normal distribution centered on the orbital response mean, while the trend component exhibits a multimodal distribution away from the standardized mean. This analysis suggests Plio-Pleistocene orbital forcing could be considered a random walk at zero-sum (the standardized mean): on long time scales, astronomical forcing oscillates around a basically time-invariant normally distributed mean of the Plio-Pleistocene climate system response. These results, consistent with those of the quantitative estimation of the variance, suggest that changes in the mean climate state during the Plio-Pleistocene were primarily caused by non-Milankovitch first-order controlling factors recorded in the global LR04 and tropical HT846 trend components (~ 76% variance). The orbital forcing acts at a hierarchically lower strength level (~ 23%), with cycles overlapping a primary trend forcing system.

Nonlinear response of $\delta^{18}O$ and SST orbital vs. trend components

Figure 10 exhibits the exponential relationships between the orbital $\delta^{18}O$ and SST components variance vs. the average $\delta^{18}O$-SST component-1 exponential fit trends by time segments binned at 532 kyr. This plot shows that the exponential increase in signal amplitude towards the Mid-Late Pleistocene is observed in all $\delta^{18}O$ and SST orbital components, from semi-precession to the eccentricity band. The exponential growth of the orbital response variance is dependent on the long-term mean climate state (LT-MCS) at a given time (mean ice volume-bottom water temperature, average sea surface-atmospheric temperature), both at a global scale (LR04) and at a local tropical scale (ODP Site 846). The exponential R^2 ranges from 0.7 to 0.9 for the $\delta^{18}O$ components and is slightly lower in the SST components (0.6 to 0.9). The minimum exponential fitting does not fall below an $R^2 = 0.64$ for SST component-2 subcomp-1-4 and $R^2 = 0.72$ for $\delta^{18}O$ component-8-11. The exponential coefficient e^{kx} for the $\delta^{18}O$ semi-precessional component is 1.05 (comp-8-11) and increases with the orbital period; it is 1.78 for the precessional component (comp-5-7), 1.88 for the obliquity component (comp-3-4), and 2.93 for the short eccentricity subcomponent (comp-2 subcomp-1-4; 9-15). The exponential coefficient is high (2.37) for the short eccentricity-obliquity modulation subcomponent (detrended comp-1 subcomp-3-11) (Fig. 10a). These data indicate an increase in $\delta^{18}O$ exponential growth from semi-precession to ~ 100-kyr eccentricity response towards the Mid-Late Pleistocene. The amplitude flattening of the obliquity-driven $\delta^{18}O$ component-3-4 during the MPT and post-MPT time shown in Fig. 4 is clearly evident in Fig. 10a also, a feature related to that observed by Lisiecki and Raymo (2007). Regarding the tropical SST, the absolute exponential coefficient e^{kx} for the semi-precessional component is 0.31 (comp-8-11). It is 0.37 for the precessional component (comp-5-7), 0.48 for the obliquity component (comp-3-4), and 0.67 for the short eccentricity subcomponent (comp-2 subcomp-1-4) (Fig. 10b). These results in tropical SST are similar to those of the global $\delta^{18}O$, although of lesser magnitude. The amplitude contraction of the obliquity-driven SST component-3-4 after the MPT start, shown in Fig. 8, is very evident even in Fig. 10b.

Figure 11 shows a quantitative analysis of the $\delta^{18}O$ and SST response modulation relative to orbital forcing as a function of the LT-MCS. The standardized response sensitivity R_s is given by the following function

$$R_s = \left(\sigma^2{}_{resp} - \sigma^2{}_{forc}\right)/\sigma^2{}_{forc} \times 100$$

where $\sigma^2{}_{resp}$ and $\sigma^2{}_{forc}$ are the variance of the standardized (0—mean; 1—standard deviation) orbital response component and forcing calculated by time segments binned at 532 kyr, respectively. For the purpose of this exercise, the eccentricity and obliquity response are approximated because small variances in these terms cannot be merged in a composite signal, or a small fraction of different frequency terms are included. Since the variance is small and the aim of this analysis is an order of magnitude estimate, the errors should be negligible. The $\delta^{18}O$ short eccentricity response (~ 6.5% variance) was considered both as a single main subcomponent (comp-2 subcomp-1-4, 9-15; 5.5% variance) containing ~ 85% of the short eccentricity response and as the weighted mean by variance of the comp-2 subcomp-1-4, 9-15 (5.5% variance) and the detrend comp-1 subcomp-3-11 (2.23% variance), the latter containing also a small fraction of long-term cycles. The $\delta^{18}O$ obliquity response (9.9% variance) was calculated as the weighted mean of the comp-3-4 (8.1%) and comp-2 subcomp-5-8 (1.8%). Similarly, the SST short eccentricity response (~ 5.1% variance) was

Table 7 Significance tests of the mean differences among $\delta^{18}O$ and SST components and the solution of orbital forcings (Laskar et al. 1993) binned at three arbitrary constant time intervals (532 kyr, 760 kyr, and 1064 kyr). Data standardized on the entire Plio-Pleistocene record (mean = 0, standard deviation = 1) and, where necessary, inverted to have the same paleoclimatic polarity (positive values for positive forcing and warming)

Component/forcing	Time bin (kyr)	Mean[a]	Sum of squares	df	*F*	Sig.
LR04 comp-1	532	− 1.47 ÷ 1.18	5059.52	9	11,504.34	0.00
	760	− 1.51 ÷ 1.13	4996.27	6	13,708.49	0.00
	1064	− 1.43 ÷ 1.14	4917.43	4	16,271.23	0.00
LR04 comp-1 subcomp-1	532	− 1.47 ÷ 1.21	5257.57	9	50,499.31	0.00
	760	− 1.50 ÷ 1.17	5182.42	6	33,599.07	0.00
	1064	− 1.44 ÷ 1.17	5116.42	4	33,559.24	0.00
LR04 comp-1 exp.fit. trend	532	− 1.72 ÷ 1.40	5262.71	9	55,162.47	0.00
	760	− 1.62 ÷ 1.35	5204.25	6	40,161.50	0.00
	1064	− 1.49 ÷ 1.28	5094.35	4	30,132.42	0.00
LR04 comp-2-11 (orbitals)	532	− 0.08 ÷ 0.09	8.80	9	0.98	0.46
	760	− 0.01 ÷ 0.02	0.74	6	0.12	0.99
	1064	− 0.01 ÷ 0.01	0.33	4	0.08	0.99
SST comp-1	532	− 1.45 ÷ 1.26	4644.74	9	6235.99	0.00
	760	− 1.42 ÷ 1.27	4468.87	6	6339.54	0.00
	1064	− 1.38 ÷ 1.16	4389.59	4	8244.21	0.00
SST comp-1 subcomp-1	532	− 1.49 ÷ 1.26	4950.98	9	24,819.72	0.00
	760	− 1.49 ÷ 1.33	4838.36	6	18,152.80	0.00
	1064	− 1.42 ÷ 1.18	4722.96	4	17,566.50	0.00
SST comp-1 exp.fit. trend	532	− 1.67 ÷ 1.50	5006.76	9	49,988.56	0.00
	760	− 1.57 ÷ 1.44	4949.41	6	36,725.39	0.00
	1064	− 1.44 ÷ 1.36	4842.28	4	27,747.29	0.00
SST comp-2-11 (orbitals)	532	− 0.09 ÷ 0.04	6.25	9	0.69	0.71
	760	− 0.01 ÷ 0.02	0.89	6	0.15	0.99
	1064	− 0.02 ÷ 0.01	0.60	4	0.15	0.96
Eccentricity	532	− 0.30 ÷ 0.25	169.60	9	19.43	0.00
	760	− 0.28 ÷ 0.28	143.98	6	24.64	0.00
	1064	− 0.22 ÷ 0.14	77.44	4	19.63	0.00
Obliquity	532	− 0.12 ÷ 0.11	35.42	9	3.96	0.00
	760	− 0.12 ÷ 0.12	37.02	6	6.21	0.00
	1064	− 0.11 ÷ 0.10	31.96	4	8.03	0.00
Precession	532	− 0.02 ÷ 0.01	0.30	9	0.03	1.00
	760	0.00	0.02	6	0.00	1.00
	1064	− 0.01 ÷ 0.01	0.12	4	0.03	1.00
65°N Insolation at June 21	532	− 0.08 ÷ 0.06	8.69	9	0.97	0.47
	760	− 0.05 ÷ 0.06	8.89	6	1.48	0.18
	1064	− 0.05 ÷ 0.04	6.37	4	1.59	0.17

df degrees of freedom, *F* Fisher test, *Sig* statistical significance
[a]Min-max of the mean among time segments

approximated as a single comp-2 subcomp-1-4 (3.65% variance) explaining ~ 72% of the short eccentricity response and as weighted mean of the comp-2 subcomp-1-4 (3.65% variance) and the detrended comp-1 subcomp-3-11 (2.84% variance), the latter containing a small fraction of long-term cycles. The weighted mean of the SST comp-3-4 (4.5% variance) and comp-2 subcomp-9-10 (0.27% variance) was calculated as the SST obliquity response, covering ~ 87% of the

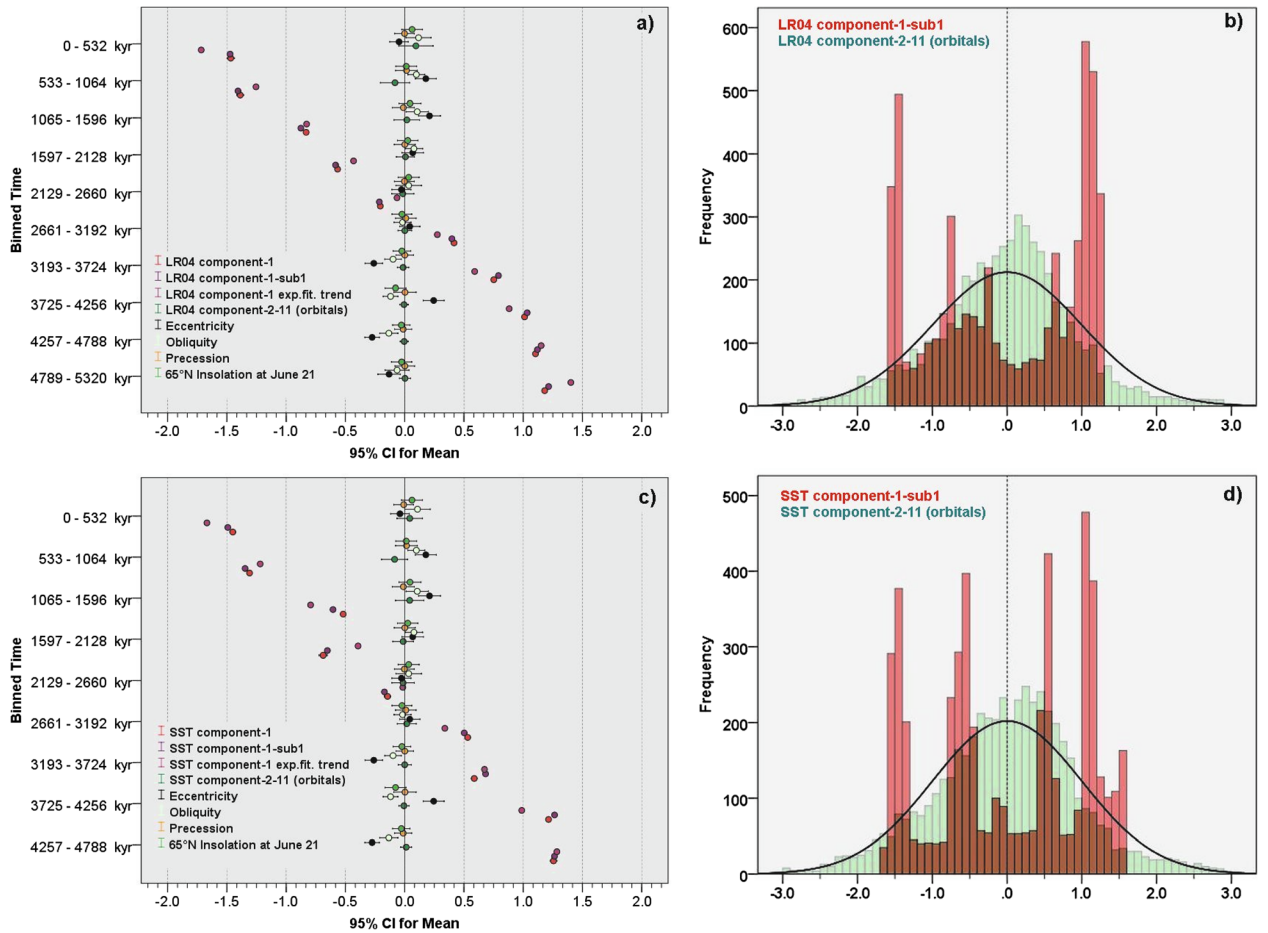

Fig. 9 Plots of the 95% confidence interval for the mean of **a** $\delta^{18}O$ components and **c** SST components compared to orbital forcings (Laskar et al. 1993), binned at 532-kyr constant time intervals. Overlapped histograms of **b** Plio-Pleistocene $\delta^{18}O$ and **d** SST orbital component-2-11 vs. trend component-1 subcomp-1. The averages of the astronomical components oscillate around the standardized mean with little statistically significance differences and a roughly normal distribution. Instead, the averages of the trend components differ very significantly, deviating markedly from the mean with a general multimodal distribution. Data standardized on the entire Plio-Pleistocene record (mean = 0, standard deviation = 1) and, where necessary, inverted to have the same paleoclimatic polarity (positive values for positive forcing and warming)

total signal (4.77% of 5.5%). A self-sustained climate system, which is only paced by orbital cycles, would produce a response sensitivity near zero because the variance of the response would match the variance in forcing, whereas values much larger than zero would indicate a nonlinear reinforcement of the signal response. Negative R_s values show a response variance lower than orbital forcing, suggesting a damping mechanism for the climate system. Figure 11a exhibits a $\delta^{18}O$ nonlinear eccentricity R_s up to 400% towards the Mid-Late Pleistocene similar to that of a precession response in shape but with a magnitude up to 200%. The two eccentricity curves are very similar, indicating a negligible error in the approximations. The $\delta^{18}O$ obliquity R_s shows a nonlinear amplification up to 180% towards the end of the MPT, followed by strong variance depletion near to zero (balance line) post-MPT. This pattern of low $\delta^{18}O$ obliquity variance is similar to that shown in Fig. 5b from Lisiecki and Raymo (2007). Remarkably, the asymptotic decay of the $\delta^{18}O$ R_s towards the Early Pliocene becomes all negative up to − 100%, suggesting a damped orbital response during the time of minimum average ice volume and higher temperature. This R_s pattern is similar considering the SST (Fig. 11b), although more scattered and with a smaller positive magnitude which does not reach 200%. The SST obliquity R_s also shows strong variance depletion up to − 20% post-MPT as well as the new feature of asymptotic decay up to − 100% of all the SST R_s towards the Early Pliocene.

Link between the pCO_2 and the SST-$\delta^{18}O$ long-term trend components

Figure 12 shows the Plio-Pleistocene cross plots among the $\delta^{18}O$, SST, and pCO_2 trend and orbital components.

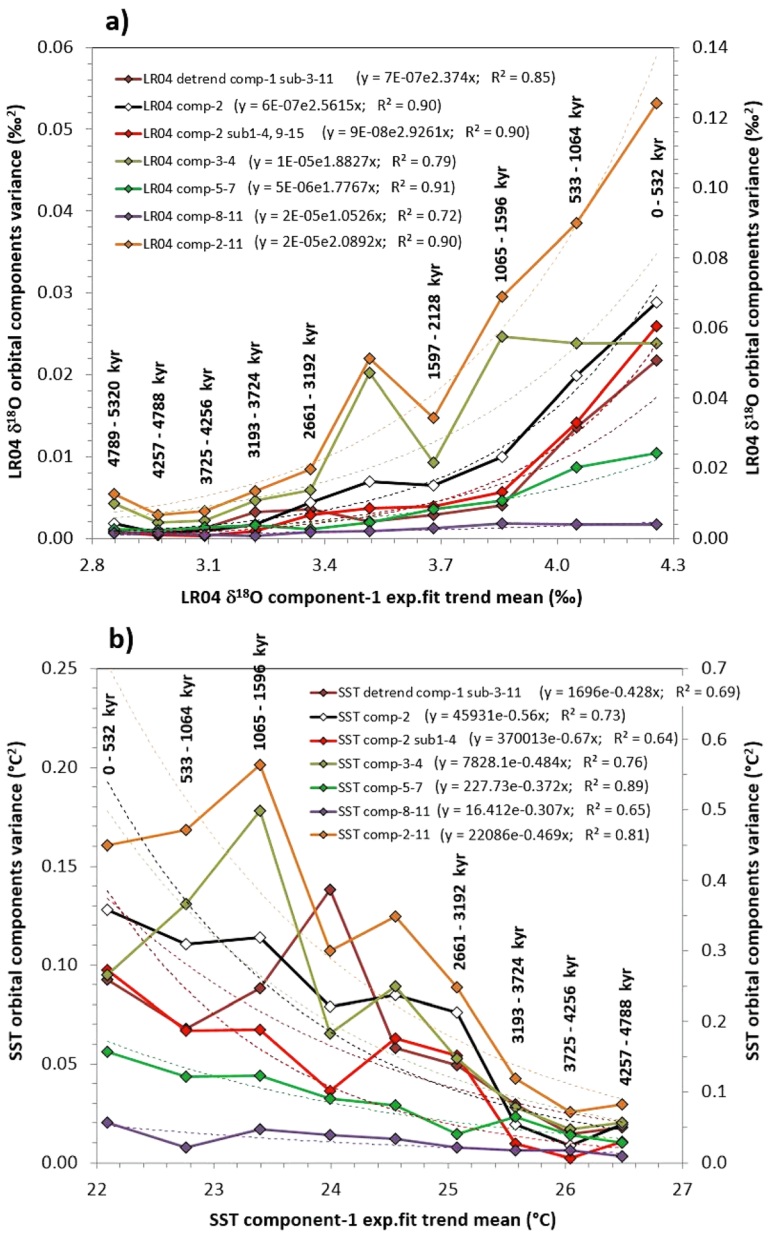

Fig. 10 Exponential relationships of the orbital variance of **a** $\delta^{18}O$ components and **b** SST components vs. the average of component-1 exponential fit trends by time segments binned at 532 kyr. The right *y*-axis shows the variance of comp-2-11 (orbitals) with a different scale to not compress the left *y*-axis values

These plots offer an overall view of the long-term trend links among the proxies. Although it is possible to express the trend relationship as exponential regressions, it was decided to use a simpler linear fitting since the correlation coefficients are similar, in order to quantify the trend rates of change. The $\delta^{18}O$ trend components exhibit a good linear interpolation vs. the boron-based pCO_2 trend of the Sites 668B-999A (Fig. 12a) and the alkenone-based pCO_2 trend of the Site 999A (Fig. 12b); differently, the $\delta^{18}O$ orbital components are unrelated to the same pCO_2 long-term trends. Similar relationships are shown by the $\delta^{18}O$ trend components and the alkenone-based SST trends of the Site 846 (Fig. 12c) and Site 999A (Fig. 12d). The tropical SST trend components of the Site 846 are linearly related to the boron-based atmospheric pCO_2 trend of the Sites 668B-999A (Fig. 12e) and the alkenone-based pCO_2 trend of the Site 999A (Fig. 12f); again, the SST orbital components are unrelated to the same pCO_2 long-term trends.

However, in the plots with more data points, the amplitude increase of the orbital components is clearly visible as pCO_2 and SST decrease, corroborating the analysis of Figs. 10 and 11. These results show that the

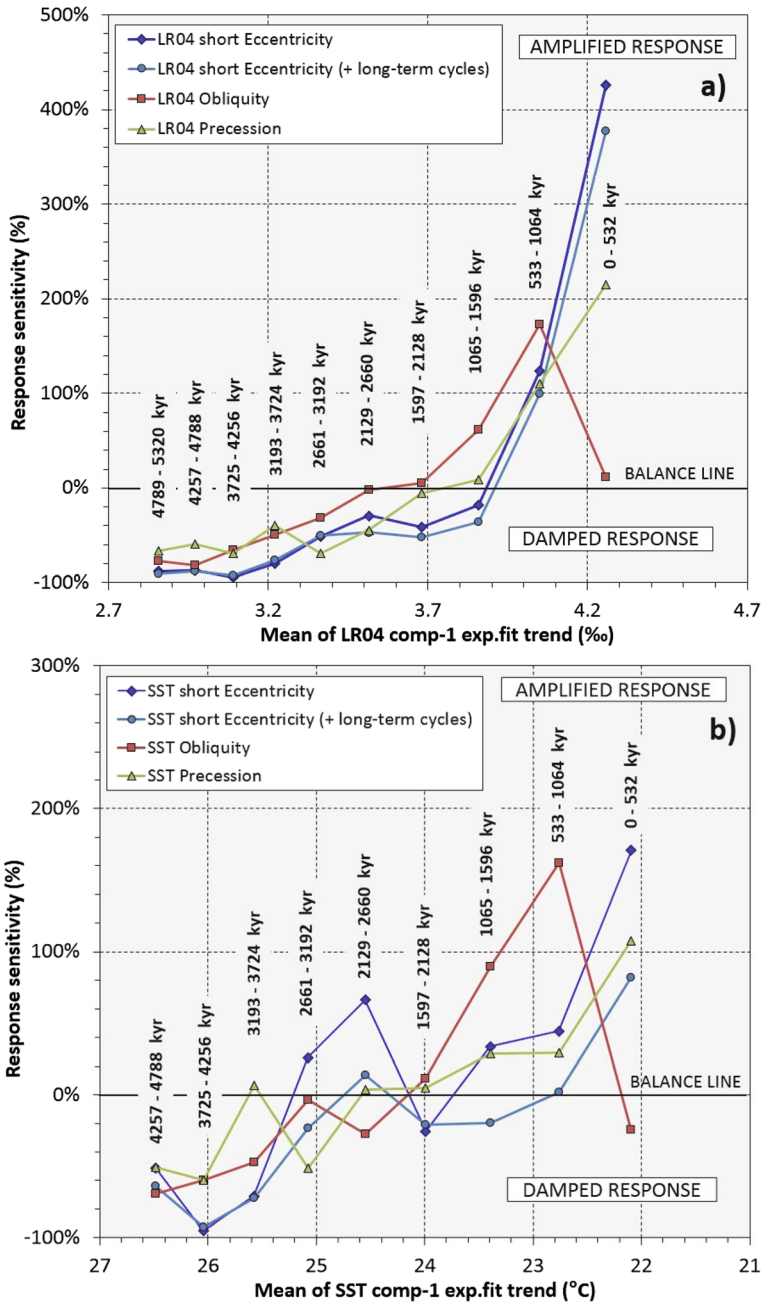

Fig. 11 Analysis of the order of magnitude in **a** $\delta^{18}O$ and **b** SST response modulation relative to orbital forcing (standardized response sensitivity R_s, see text) as a function of the LT-MCS. The balance line (0%) indicates that the variance of response matches the variance in forcing, suggesting a self-sustained climate system, which is only paced by orbital cycles. Values much larger than zero would indicate a nonlinear reinforcement of the signal response. Negative R_s shows a response variance lower than orbital forcing, suggesting a damping mechanism for the climate system

climate sensitivity to orbital forcing is lower when CO_2 and SST are higher (Early Pliocene) and that it increases non-linearly when CO_2 and SST are low (Mid-Late Pleistocene), in agreement to Martinez-Boti et al. (2015), a feature linked to the LT-MCS as shown in the present study. Despite that Site 846 is considered not "typical" tropical SST record, Fig. 13a shows a very close link between its trend component and that of the global ΔSST stack (Martinez-Boti et al. 2015) identified by SSA and driving 76.2% of the variance (ΔSST comp-1), noteworthy the same magnitude of the Site 846 SST and global $\delta^{18}O$ trend components (76.6% and 76.4%, respectively). The inclusion of the Site 846 among the ten of the ΔSST stack should not significantly affect the

global character of the signal. Moreover, Lisiecki (2010b) calculates 0.28 °C/Myr the upwelling cooling effect at Site 846 which roughly matches a 30% fraction of the total 1.0 °C/Myr trend (Herbert et al. 2010a), resulting about 70% of the Site 846 cooling trend to be due to non-regional effects, according to the results of the SSA.

Figure 13 shows similar links of Fig. 12 among the global ΔSST long-term trend and the pCO_2 trends at Sites 668B and 999A (Fig. 13c) and 999A (Fig. 13d) and the global $\delta^{18}O$ (Fig. 13b). Figure 13e, f exhibits the same relationships by converting the standardized ΔSST into SST (°C) using the function of Fig. 13a. The SST vs. boron-based CO_2 trend slopes correspond to a tropical rate of change of 25.6 μatm/°C (Fig. 12e), very close to the global converted ΔSST stack of 25.5 μatm/°C (Fig. 13e). At 25 °C and atmospheric pressure, these values are equivalent to a rate of change of 26.4 ppm/°C and 26.3 ppm/°C, respectively. Coherently, as shown in Fig. 14b, the two SST trends are subparallel in time, although the Site 846 is cool-shifted. Considering the alkenone-based CO_2 trend slopes, these rates of changes are of 42.6 ppm/°C (Fig. 12f) and 39.2 ppm/°C (Fig. 13f), respectively. Such variability in rate of changes (~ 26 ppm/°C vs. ~ 41 ppm/°C) could be due to differences in the CO_2 proxy estimation (boron-based vs. alkenone-based). These slope data offer an overall view of the Plio-Pleistocene long-term climate sensitivity, and the oscillations around the linear trend should indicate that it can change for discrete time intervals. On the other hand, the climate sensitivity to orbital forcing change by time in response to the initial conditions set by LT-MCS (Tachikawa et al. 2014; Martinez-Boti et al. 2015; Lo et al. 2017; this study).

These results authorize to be considered of global in nature the non-Milankovitch trend links among pCO_2, SST, and $\delta^{18}O$. Considering that the main GHGs, such as carbon dioxide and methane, operate physically as the most effective positive (warming) climate forcings (Hansen et al. 2005; Hansen and Sato 2012; Van Der Meer et al. 2014), the hypothesis that the global long-term variation of atmospheric GHG concentration plays a relevant role in explaining the origin of the $\delta^{18}O$ and SST trend components, driving ~ 76% of the Plio-Pleistocene signal variance, appears plausible.

Figure 14 shows the correlation over time between the $\delta^{18}O$ enrichment trend components (LR04 comp-1 subcomp-1 and LR04 comp-1 exponential fit) and the CO_2 reduction trend of the ODP Sites 668B and 999A (Fig. 14a) and the SST cooling trends of the global ΔSST stack, ODP Sites 846 and 999A (Fig. 14b).

During the Zanclean, the pCO_2 alkenone ranged from 450 to 330 ppm, the highest values of the entire Plio-Pleistocene; the tropical SST was higher than the Plio-Pleistocene average; and the global $\delta^{18}O$ was depleted more than the average (Fig. 14). Conversely, the mean orbital forcing was slightly negative (Fig. 9). These observations indicate Zanclean as a period of a higher than average positive climate state, supporting the hypothesis that the Zanclean warmer climate may have been driven by an important greenhouse effect due to higher atmospheric CO_2 (Bartoli et al. 2011). The lack of significant Northern Hemisphere ice growth and 100-kyr climate response prior to 3.3 Myr suggest that pCO_2 alkenone above 320–330 ppm is associated with warming sufficient to prevent significant Northern Hemisphere ice sheet growth even during cold orbital phases (Seki et al. 2010). The pCO_2 and SST show a significant reduction during the Zanclean (subtrend-I), supporting the hypothesis that the ONHG was triggered by the decreasing trend in atmospheric CO_2 (Pagani et al. 2010; Seki et al. 2010). Subtrend-II (Piacenzian) is also consistent with a reduction of pCO_2 alkenone and SST, suggesting an INHG triggered by a further decrease in atmospheric CO_2 according to Lunt et al. (2008), who stated that Greenland glaciation was primarily controlled by a decrease in atmospheric CO_2 during the Late Pliocene. Nevertheless, the Piacenzian remains a period of a $\delta^{18}O$-SST higher than average positive climate state, with slightly negative or neutral mean orbital forcing (Fig. 9). For this reason, the Piacenzian, excluding the ONHG event, is still characterized by an average warming fingerprint due to a residual greenhouse effect. According to this hypothesis, Lunt et al. (2012), using a modeling approach, showed that on a global scale, the largest contributor to mid-Piacenzian warmth (3.26–3.03 Myr) is high CO_2. Subtrend-III (Gelasian-Calabrian p.p.) does not appear to comply with the pCO_2 alkenone data, probably due to the low-resolution proxy in this range, while it is more consistent with the decreasing boron-based pCO_2 and the SST subtrends. For the first time during the Plio-Pleistocene, the long-term $pCO_2$and SST are below or close the mean and the $\delta^{18}O$ is enriched more than the average (Figs. 14 and 9). The mean orbital forcing is neutral or slightly positive. The net result of these two unbalanced forcings may be a significant cooling effect and the start of an average "icehouse" world. Subtrend-IV (Calabrian-Middle Pleistocene p.p.) is consistent with a further reduction of pCO_2, reaching peak concentrations of 240–250 ppm (MIS-16), and with the continuation of the SST cooling trend. The long-term pCO_2, SST, and $\delta^{18}O$ are consolidated below the mean, while the mean orbital forcing appears slightly positive, resulting in a lower than average negative climate state, strengthening the icehouse effect. No CO_2 variation corresponds to the MPT, although it falls at the beginning of subtrend-IV after a long time interval of surface/deep-water cooling and ice volume growth. Finally, the MBO (Mid-Late Pleistocene) marks a mild recovery of the long-term pCO_2 clearly visible in the EPICA trend comp-1

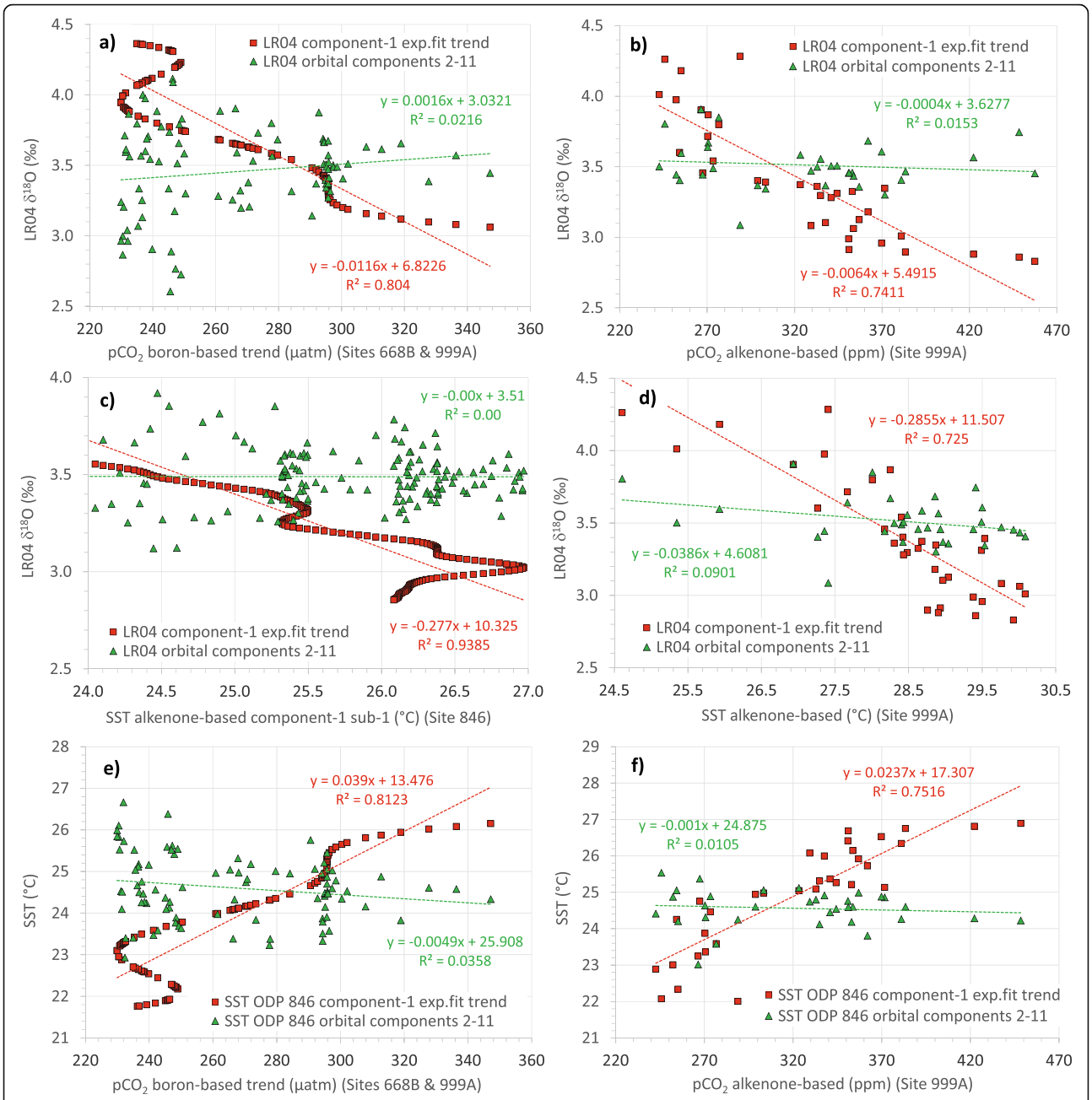

Fig. 12 Plio-Pleistocene cross plots between selected pCO_2 proxies and the $\delta^{18}O$ (**a**, **b**) and SST (**e**, **f**) SSA-components. Plio-Pleistocene cross plots between selected SST proxies and the $\delta^{18}O$ (**c**, **d**) SSA-components. A clear linear interpolation is shown between long-term trend components, whereas orbital components-2-11 are unrelated to the long-term trends. Proxy data: composite atmospheric boron-based pCO_2 proxy from ODP Sites 668B-999A (Hönisch et al. 2009; Bartoli et al. 2011), atmospheric alkenone-based pCO_2 and SST proxies from ODP Site 999A (Seki et al. 2010), alkenone-based SST proxy from ODP Site 846 (Herbert et al. 2010b), and LR04 $\delta^{18}O$ stack (Lisiecki and Raymo 2005b)

subcomp-3 and less distinctly in the CO_2 proxy records (see Additional file 1) (Lisiecki 2010b; Seki et al. 2010) and in the SST proxies (Fig. 14). The strong isotopic enrichment related to MIS-16 at the end of the subtrend-IV correlates well with the absolute CO_2 minimum in the EPICA comp-1 subcomp-3 at ~ 0.65 Myr. Considering that the $\delta^{18}O$ response lags CO_2 (Shackleton 2000; this study), the correlation between the CO_2 maximum in the EPICA comp-1 subcomp-3 at ~ 0.4 Myr and the related but slightly delayed isotopic depletion in the $\delta^{18}O$ comp-1 subcomp-1 is noteworthy (MBO). This observation supports the hypothesis that MIS-11, one of the most intense and prolonged interglacial oscillations of the Middle-Late Pleistocene, which is not proportional to eccentricity (Imbrie et al. 1993)

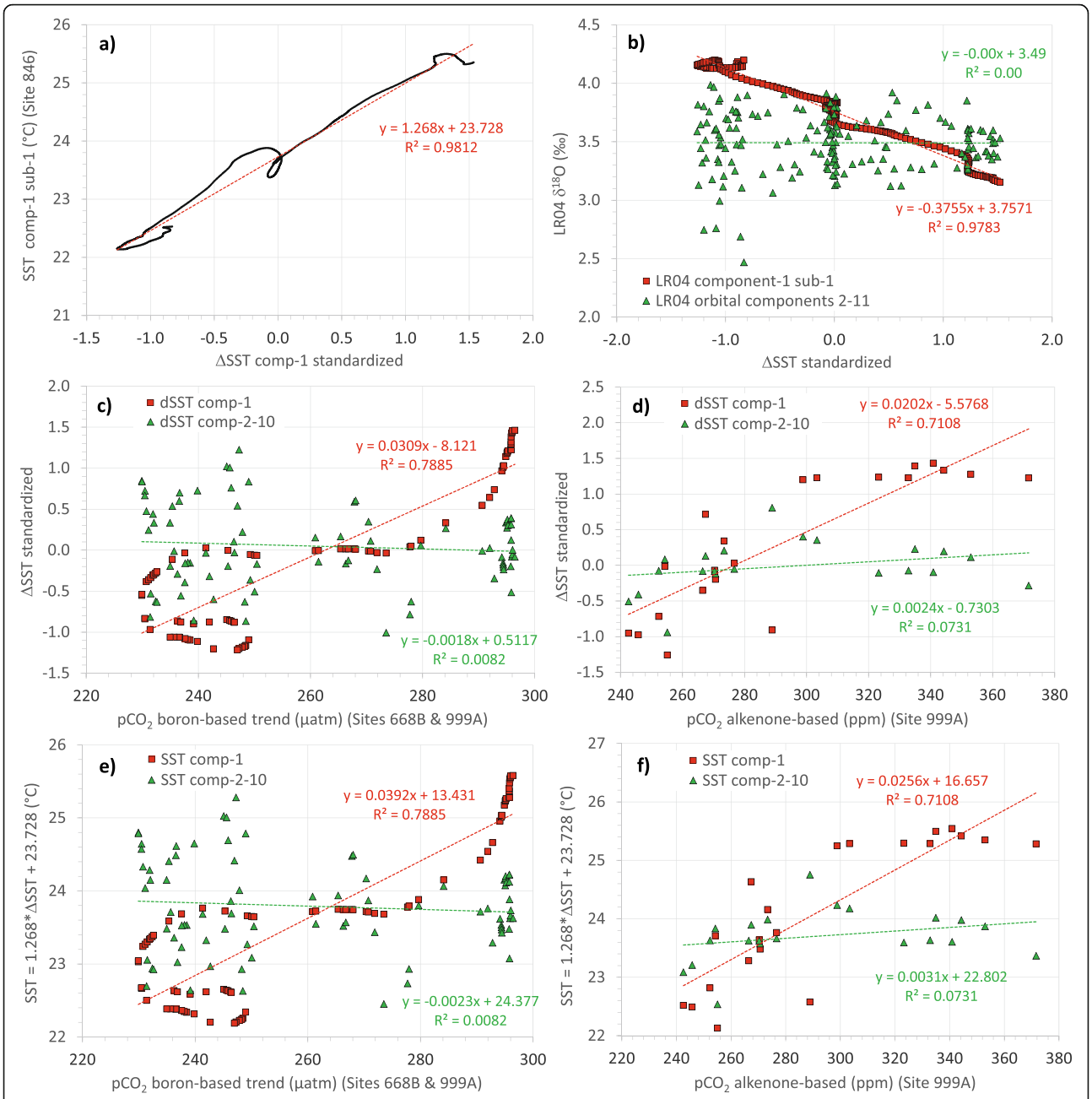

Fig. 13 Late Pliocene-Pleistocene cross plot between trend components of global ΔSST stack and tropical SST at Site 846 (**a**). Cross plots between the ΔSST stack and **b** $\delta^{18}O$, **c** boron-based, and **d** alkenone-based pCO_2 SSA-components. Cross plots between the converted ΔSST stack (°C by means of the function in **a**) and **e** boron-based pCO_2 and **f** alkenone-based pCO_2 trends. The long-term trend components are clearly linked, whereas orbital components are unrelated to the long-term trends. Proxy data: composite atmospheric boron-based pCO_2 proxy from ODP Sites 668B-999A (Hönisch et al. 2009; Bartoli et al. 2011), atmospheric alkenone-based pCO_2 and SST proxies from ODP Site 999A (Seki et al. 2010), alkenone-based SST proxy from ODP Site 846 (Herbert et al. 2010b), LR04 $\delta^{18}O$ stack (Lisiecki and Raymo 2005b), and global ΔSST stack (Martinez-Boti et al. 2015)

or cool insolation-induced interglacials (Berger et al. 2012), may be an astronomical event boosted by GHG mid-term recovery, which reached the highest value at ~400 kyr (Luthi et al. 2008; Berger and Yin 2012; Berger et al. 2016). The origin of this GHG mid-term recovery could be partly due to the long-term orbital cycles that reach a maximum relative (warming) at ~300–200 kyr (Figs. 2 and 6); the 400-kyr eccentricity cycle really reaches a maximum at about 200 kyr (Laskar et al. 2011). However, the timing of these astronomical events does not seem consistent with the CO_2 maximum of EPICA at ~400 kyr. In addition, we cannot exclude a contribution of the circum-Pacific explosive activity (Jicha et al. 2009). The Late Pleistocene was a period of quiescence of the circum-Pacific explosive activity,

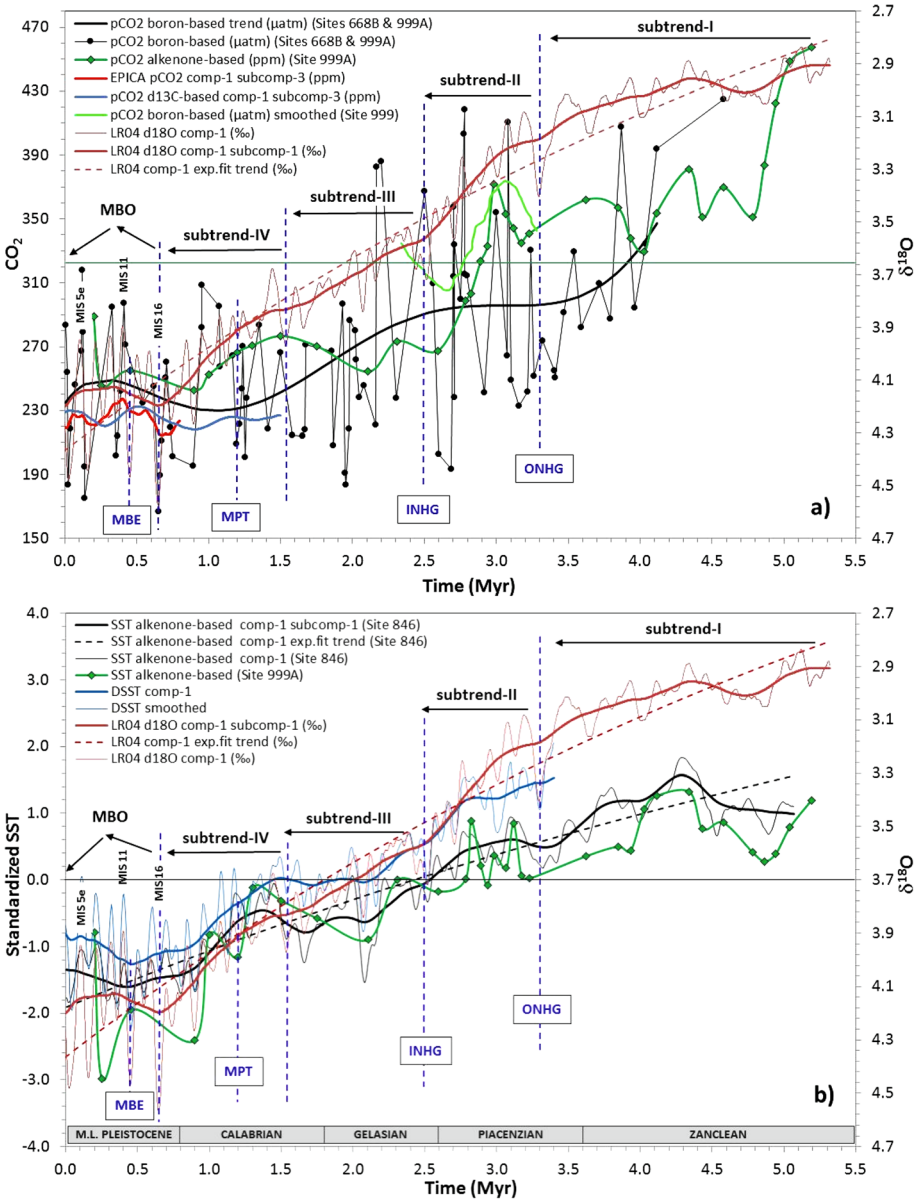

Fig. 14 Comparison over time of the long-term trend components of $\delta^{18}O$ and the **a** pCO_2 and **b** SST proxies. Composite atmospheric boron-based pCO_2 proxy from ODP Sites 668B-999A (Hönisch et al. 2009; Bartoli et al. 2011), atmospheric alkenone-based pCO_2 and SST proxies from ODP Site 999A (Seki et al. 2010), alkenone-based SST proxy from ODP Site 846 (Herbert et al. 2010b), EPICA pCO_2 record (Berger et al. 2016), $\delta^{13}C$-based pCO_2 proxy (Lisiecki 2010b), LR04 $\delta^{18}O$ stack (Lisiecki and Raymo 2005b), boron-based pCO_2 proxy from ODP Site 999 and global **Δ**SST stack (Martinez-Boti et al. 2015). The horizontal lines are the Plio-Pleistocene average of pCO_2 alkenone (ODP Site 999A) and the standardized mean of the SST. All records are plotted on their own age scale

which perhaps contributed to the mid-term CO_2 increment by a reduction in volcanic aerosols and the consequent minor algal ash-fertilization of the Pacific Ocean waters (Jicha et al. 2009).

Lagged patterns of $\delta^{18}O$ and SST orbital components

The phase relationships between the standardized La93 orbital forcings and the orbitally driven LR04-SST components are shown in Table 8 for three time intervals. The results indicate that the $\delta^{18}O$ and SST orbital components are all delayed on average compared to the related forcing of eccentricity, obliquity, and precession (with the small significant exception of the eccentricity in the pre-ONHG time due to very low SST signal coherency), although the patterns of coherency and phase lag are quite different across the time intervals.

These cross-spectral results are in general agreement with Imbrie et al. (1993), Shackleton (2000), Lisiecki and

Raymo (2005a), and Tziperman et al. (2006) and indicate that the climate system takes a certain amount of time to transfer the effect of orbital forcing to the global ice volume/deep water temperature and to the sea surface temperature. The coherency is generally lower in the tropical SST signal probably due to differences in the forcings controlled by high-latitude and low-latitude signals. The lagging of the $\delta^{18}O$ signal is usually larger than that of the SST (Table 8) because the ice volume component lags the deep water temperature signal in the $\delta^{18}O$ record (Lisiecki and Raymo 2005a; Herbert et al. 2010a). The coherency of the eccentricity signal increases from pre-ONHG time (incoherent) towards the Mid-Late Pleistocene, reflecting the progressive increase of eccentricity power both in global $\delta^{18}O$ and local tropical SST signals. The delta-lag in eccentricity between $\delta^{18}O$ and SST reaches its maximum during the Late Pleistocene (4.31–0.44 kyr), suggesting an increased contribution of the $\delta^{18}O$ ice volume component over the water temperature signal. The $\delta^{18}O$ and SST obliquity signals have the largest coherency and exhibit an average increasing trend in the lags towards the Mid-Late Pleistocene, starting from 4.10–3.46 kyr to 5.78–5.28 kyr and, finally, reaching values of 7.42–2.71 kyr (Table 8), in general agreement with Lisiecki and Raymo (2005a). The $\delta^{18}O$-SST delta-lag in obliquity is relatively small until

Table 8 Cross-spectral analysis results among the orbital forcings (Laskar et al. 1993) and the orbitally driven $\delta^{18}O$ and SST components for three time intervals. Data standardized (mean = 0, standard deviation = 1) and, where necessary, inverted to have the same paleoclimatic polarity (positive values for positive forcing and warming)

Time interval	Orbital forcing	Response component	Cross-spectrum freq. (kyr^{-1})	Cross-spectrum period (kyr)	Coherency	Phase shift		
Post-MPT start	Eccentricity	LR04 comp-2 subcomp-1-4, 9-15	0.010742	93	0.72	− 16.65°	− 4.31 kyr	$\delta^{18}O$ component lags eccentricity
		SST comp-2 subcomp-1-4	0.010742	93	0.70	− 01.70°	− 0.44 kyr	SST component lags eccentricity
	Obliquity	LR04 comp-3-4	0.024414	41	0.93	− 65.20°	− 7.42 kyr	$\delta^{18}O$ component lags obliquity
		SST comp-3-4	0.024414	41	0.68	− 23.78°	− 2.71 kyr	SST component lags obliquity
	Precession	LR04 comp-5-7	0.041992	24	0.78	− 74.50°	− 4.93 kyr	$\delta^{18}O$ component lags precession
		SST comp-5-7	0.041992	24	0.72	− 53.24°	− 3.52 kyr	SST component lags precession
ONHG-MPT start	Eccentricity	LR04 comp-2 subcomp-1-4, 9-15	0.010742	93	0.47	− 27.57°	− 7.13 kyr	$\delta^{18}O$ component lags eccentricity
		SST comp-2 subcomp-1-4	0.010742	93	0.45	− 21.37°	− 5.53 kyr	SST component lags eccentricity
	Obliquity	LR04 comp-3-4	0.024414	41	0.98	− 50.79°	− 5.78 kyr	$\delta^{18}O$ component lags obliquity
		SST comp-3-4	0.024658	41	0.95	− 46.85°	− 5.28 kyr	SST component lags obliquity
	Precession	LR04 comp-5-7	0.044678	22	0.89	− 57.37°	− 3.57 kyr	$\delta^{18}O$ component lags precession
		SST comp-5-7	0.042236	24	0.28	− 119.35	− 7.85 kyr	SST component lags precession
Pre-ONHG	Eccentricity	LR04 comp-2 subcomp-1-4, 9-15	0.009766	102	0.32	− 01.48°	− 0.42 kyr	$\delta^{18}O$ component lags eccentricity
		SST comp-2 subcomp-1-4	0.010742	93	0.13	+ 07.06°	1.83 kyr	SST component leads eccentricity
	Obliquity	LR04 comp-3-4	0.024414	41	0.95	− 36.02°	− 4.10 kyr	$\delta^{18}O$ component lags obliquity
		SST comp-3-4	0.024414	41	0.81	− 30.42°	− 3.46 kyr	SST component lags obliquity
	Precession	LR04 comp-5-7	0.042480	24	0.42	− 88.11°	− 5.76 kyr	$\delta^{18}O$ component lags precession
		SST comp-5-7	0.042480	24	0.59	− 87.60°	− 5.73 kyr	SST component lags precession

the beginning of the MPT and becomes large after this transition, probably following global ice volume growth. The cross-spectral results relative to precession are more variable. The precession lag is basically constant (5.76–5.73 kyr) during pre-ONHG time, then it becomes quite "unstable" (3.57–7.85 kyr) between ONHG and MPT and reaches lags of 4.93–3.52 kyr post-MPT. The minimum $\delta^{18}O$ phase lag relative to precession (3.57 kyr) during the ONHG-MPT time interval suggests the influence of a large global deep water temperature signal (Lisiecki and Raymo 2005a). During the same time interval, the precession's SST lag reached its maximum (7.85 kyr) which could be due to the effect of a deep water upwelling in the EEP (ODP Site 846). Table 9 exhibits, for the last 5 Myr, the cross-spectral analysis results between SST and LR04 orbital components, showing a slight $\delta^{18}O$ lagged response vs. SST, in agreement with Herbert et al. (2010a). The slightly earlier response of the $\delta^{18}O$ eccentricity component (0.05 kyr) is due to the pre-ONHG weak and unstable eccentricity signal. After the ONHG, the eccentricity response is strengthened and becomes more stable resulting in a slight $\delta^{18}O$ lag.

Discussion

Origin of the $\delta^{18}O$ and SST trend components

The LR04 trend component is related to the Plio-Pleistocene interval of the Cenozoic $\delta^{18}O$ enrichment trend starting at the end of the Early Eocene Climatic Optimum (EECO, 53–51 Myr), documenting the progressive development of the Antarctic and Boreal ice sheets (Zachos et al. 2001). The gradual climate cooling during the Cenozoic is generally correlated to a CO_2 concentration decrease in the atmosphere (Raymo and Ruddiman 1992; Zachos et al. 2001; Royer 2006; Zachos et al. 2008; Van de Wal et al. 2011; Zhang et al. 2013; Van Der Meer et al. 2014). Recent studies on Pliocene and Pleistocene alkenone $\delta^{13}C$ and boron-based pCO_2 proxies support this hypothesis (Seki et al. 2010; Pagani et al. 2010; Bartoli et al. 2011). Stap et al. (2014) find that the atmospheric temperature during the past 800 kyr has been controlled by a complex interaction of CO_2 and insolation, and both variables serve as thresholds for the NHG. Using CO_2 proxies and geochemical carbon cycle models, Royer (2006) shows that atmospheric CO_2 exhibits a pervasive and tight positive correlation with globally averaged surface temperatures, indicating that CO_2 played a strong role in driving the global climate for much of the Phanerozoic. The Cenozoic climatic record provides an important case study to understand the relationships between carbon cycling and climate (Zachos et al. 2001, 2008). In fact, much of the early Cenozoic was characterized by noticeably higher concentrations of GHGs and a much warmer mean global temperature. The most extreme event being between 53 and 51 Myr (EECO), when CO_2 concentration was on the order of 1000–1500 ppm, and the global temperatures reached a long-term Cenozoic maximum (Zachos et al. 2001, 2008; Beerling and Royer 2011). Zhang et al. (2013) estimate the new pCO_2 data for the Middle Miocene to be notably higher than published records with average pCO_2 concentrations in the range of 400–500 ppm, suggesting that CO_2 levels were highest during a period of global warmth associated with the Middle Miocene Climatic Optimum (MMCO, 17–14 Myr). Instead, during the mid-Pleistocene ice ages, CO_2 fell to 170–190 ppm, and the global temperature reached a long-term Cenozoic minimum (Beerling and Royer 2011; Berger et al. 2016). Considering a CO_2 variation from approximately 1000 ppm in the early Cenozoic to 170 ppm in the icy Pleistocene, the resulting negative climate forcing computed by Hansen and Sato (2012) for this CO_2 range exceeded 10 W/m^2, which is consistent with the observed strong Cenozoic cooling. These studies confirm the link among global temperature, the cryosphere, and atmospheric CO_2. The present study suggests a link between the

Table 9 Cross-spectral analysis results between orbitally driven $\delta^{18}O$ and SST components for the last 5 Myr. Data standardized (mean = 0, standard deviation = 1) and, where necessary, inverted to have the same paleoclimatic polarity (positive values for positive forcing and warming)

SST component	$\delta^{18}O$ component	Cross-spectrum freq. (kyr^{-1})	Cross-spectrum period (kyr)	Coherency	Phase shift		
SST comp-2 subcomp-1-4	LR04 comp-2 subcomp-1-4, 9-15	0.010498	95	0.89	0.20°	0.05 kyr	$\delta^{18}O$ leads SST eccentricity comp.
SST comp-2 subcomp-1-4 (post-ONHG)	LR04 comp-2 subcomp-1-4, 9-15 (post-ONHG)	0.010498	95	0.84	− 0.38°	− 0.10 kyr	$\delta^{18}O$ lags SST eccentricity comp.
SST comp-3-4	LR04 comp-3-4	0.024414	41	0.92	− 24.57°	− 2.80 kyr	$\delta^{18}O$ lags SST obliquity comp.
SST comp-5-7	LR04 comp-5-7	0.044800	22	0.46	− 16.40°	− 1.02 kyr	$\delta^{18}O$ lags SST precession comp.

atmospheric pCO_2 long-term variations and the SST-$\delta^{18}O$ trend components and highlights the primary role of the long-term change of the atmospheric GHG concentration in explaining the origin of the high-variance, highly significant $\delta^{18}O$ and SST trend components.

Factors controlling long-term atmospheric composition

Although it is generally accepted that the progressive Cenozoic cooling of the global climate resulted from a long-term decrease in atmospheric CO_2, details on how carbon cycle affects CO_2 and a clearer distinction of the involved time scales have not been fully resolved. Because of the relatively small size of the atmospheric reservoir, minimal imbalances between CO_2 sources and sinks cause rapid fluctuations in atmospheric CO_2 levels and global mean temperatures (Brady and Gislason 1997; Kent and Muttoni 2013). The results of the present study suggest ~ 76% of the Plio-Pleistocene climate variance could be driven by non-orbital carbon cycle. On time scales longer than one million years, atmospheric CO_2 levels are primarily controlled by the balance between the rate of volcanic and metamorphic sources from the Earth's interior and the rate of sink through the chemical weathering of silicate minerals and through the burial of organic carbon (Walker and Hays 1981; Berner et al. 1983; Raymo and Ruddiman 1992; Brady and Gislason 1997; Schrag et al. 2002; Hansen and Sato 2012). Plate tectonics may affect the primary inputs of atmospheric CO_2 through mantle outgassing at seafloor spreading ridges, volcanoes, and the metamorphism of carbonate rocks along subduction zones (Van Der Meer et al. 2014). Long-term sinks for CO_2 are controlled by the burial of organic matter and by the weathering of silicate rocks to form carbonates (Raymo and Ruddiman 1992; Berner and Kothavala 2001; Schrag et al. 2002; Van Der Meer et al. 2014). The weathering of silicate rocks is a chemical process whereby CO_2 consumption is buffered by the temperature dependence on the weathering rate, preventing the so-called "ice catastrophe" when temperatures fall (Walker and Hays 1981). As the atmospheric CO_2 concentration rises, the temperature and precipitation increase. They thereby enhance chemical weathering and atmospheric CO_2 depletion, preventing "greenhouse" disasters on geological timescales. Chemical weathering is also affected by changes in continental land area and paleoaltitude distribution (Berner et al. 1983; Schrag et al. 2002). The alteration of surficial marine basalts at low temperatures (< 40 °C) is another potentially important sink for atmospheric CO_2 over geologic time (Brady and Gislason 1997). The numerical modeling of the carbon cycle by Berner et al. (1983) suggests that changes in volcanic outgassing over the last 100 million years were the primary cause of the transition between the greenhouse climates of the Cretaceous and the ice ages of the Plio-Pleistocene. Their results indicate that the CO_2 content in the atmosphere is highly sensitive to changes in the seafloor spreading rate and continental land area. A tropical concentration of continental area may lead to a more efficient burial of organic carbon through increased tropical river discharge and the chemical weathering of silicate rocks (Schrag et al. 2002). By affecting CO_2 volcanic degassing, metamorphic-magmatic decarbonation and changes in the continental land area available for chemical weathering, plate tectonics is considered the main long-term controlling factor of the global climate (Berner et al. 1983; Van Der Meer et al. 2014). However, it is a matter of debate as to which main mechanism can adjust the balance between the CO_2 source through geotectonic volcanic degassing and the CO_2 sink by the chemical weathering of silicate rocks. Some studies show conflicting results regarding the role of the seafloor spreading rate, which is believed to be the major control of CO_2 degassing (Berner et al. 1983; Raymo and Ruddiman 1992). In fact, according to Rowley (2002), the seafloor spreading rate remained relatively constant over the past 180 Myr, while Cogné and Humler (2006) indicate a general increasing trend in the last 50 Myr. These results are discordant with the observed cooling trend of the Cenozoic climate. Recently, a study of carbon-cycle evolution indicated that increasing physical erosion in response to widespread mountain building is the most prominent driver of carbon cycling over the past 100 Myr (Li and Elderfield 2013). Raymo and Ruddiman (1992) proposed that the uplift of the Tibetan plateau was an important driving force behind the Cenozoic long-term cooling by atmospheric CO_2 consumption due to the increase of the chemical weathering of silicate rocks. However, the Cenozoic long-term shift in Earth's climatic state could be really related to regional transient differences in volcanic emissions by plate tectonic activity, which were particularly high during, e.g., the Late Paleocene and Early Eocene epochs (North Atlantic rifting and India-Asian northward migration) (Raymo and Ruddiman 1992; Zachos et al. 2001; Mosar et al. 2002; Zachos et al. 2008; Le Breton et al. 2012). From this viewpoint, a recent study on the Himalayan-Tibetan orogenic system shows a multiple collision model in which a continent-continent collision began around the Eocene/Oligocene boundary (34 Myr) (Aitchison et al. 2007), promoting the Early Oligocene glaciation (Zachos et al. 2001). Corroborating this hypothesis, the North Atlantic seafloor spreading rate (NASSR) exhibits a clear decreasing trend from high values in the Early Eocene (55–50 Myr) to a very low rate for most of the Oligocene (Mosar et al. 2002; Le Breton et al. 2012). On the other hand, recent studies seem to converge towards a significant 250–200-Myr period variation of the seafloor spreading rate

(Becker et al. 2009; Coltice et al. 2013). Becker et al. (2009) proposed a spreading rate long-term slowdown since 140 Myr with minor cycles superimposed over time, such as a relative increase at ~ 50 Myr and a minimum at ~ 32 Myr. Even the timing of the global average spreading rate (GASR) calculated by Conrad and Lithgow-Bertelloni (2007) appears to support the hypothesis of a direct geotectonic "forcing" to the long-term composition of atmospheric GHGs. On a more detailed timescale, a study in the North Atlantic shows the consistency of the NASSR relative maximum at ~ 15 Myr and the MMCO (Merkouriev and DeMets 2014). The correlation of the NASSR minimum at approximately 1.2–1.0 Myr (the lowest value in the last 20 Myr) and the CO_2 proxy minimum at 0.9–0.7 Myr (Fig. 14a), which correlate to the strong LT-LR04 cooling at the end of subtrend-IV, seems plausible. Indeed, the contribution of the important negative forcing created by aerosols (Hansen et al. 2005) emitted into the atmosphere during phases of explosive volcanic paroxysm in the circum-Pacific (Jicha et al. 2009) must also be taken in account. In fact, hundreds of explosive eruptions occurred during an extremely vigorous period of circum-Pacific volcanism beginning in the Late Eocene, which likely led to the production of sulfur aerosols in the stratosphere and net cooling. The feedback mechanism related to the enormous supply of ash that fertilized the Pacific Ocean waters might have caused algal growth and CO_2 uptake and thereby contributed to Oligocene glaciation at approximately 34 Myr (Jicha et al. 2009). It is interesting to observe how the Plio-Pleistocene in the circum-Pacific was a period of intense explosive volcanic activity characterized by three activity peaks at approximately 4.8, 2.8, and 1.5 Myr (Jicha et al. 2009). We cannot exclude that these events contributed in part to the three most pronounced segments of $\delta^{18}O$ enrichment highlighted in the LT-LR04 record (subtrend-I, subtrend-II, and subtrend-IV), culminating in the ONHG, INHG, and MIS-16 events, respectively. Moreover, the Late Pleistocene was a period of quiescence of the circum-Pacific explosive activity, which may have contributed to the mid-term CO_2 increment and $\delta^{18}O$ impoverishment that occurred at approximately 400–300 kyr, a possible cause of the MBO. A further contribution to the global emission of CH_4 and CO_2 may also come from the thermogenic cracking of organic carbon-rich sediments in large igneous provinces (LIPs), which are associated with geotectonic spreading areas or subduction zones (Svensen et al. 2004). Finally, another climate-controlling factor is oceanic paleocirculation. The "Panama Hypothesis" states that the gradual closure of the Panama seaway, between 13 and 2.6 Myr led to a decreased mixing of the Atlantic and Pacific water masses and a strengthening of the Atlantic thermohaline circulation, increased temperatures and precipitation in Northern Hemisphere high latitudes, and culminated with the INHG during the Pliocene, at approximately 3.2–2.7 Myr (Bartoli et al. 2005; Lunt et al. 2008). However, Lunt et al. (2008), using a more sophisticated general circulation model (GCM), demonstrated that the ice volume difference between the "closed" and "open" seaway model configurations is small and concluded that it was not a major forcing mechanism. This view accommodates $\delta^{18}O$ and SST components-8-11 of inter-tropical semi-precessional origin related to the oceanic heat transport towards high latitudes (Hagelberg et al. 1994; Berger et al. 2006), which contributes very little to the total variance of the paleoclimatic response (~ 0.6–0.5%). In summary, the geotectonic forcing appears a plausible hypothesis to explain the long-term changes in atmosphere composition (GHGs and volcanic aerosols) through direct (CO_2 outgassing and explosive volcanism) and indirect (orography and erosion, paleogeographic configuration, oceanic paleocirculation, and ocean fertilization) control by plate tectonics.

Nonlinear response and mean climate state

An interesting result of the present study shows that the nonlinear increase in signal amplitude from the Early Pliocene to the Late Pleistocene is observed in all $\delta^{18}O$ and SST astronomical components and is exponentially linked to the LT-MCS (Figs. 10 and 11). These results reinforce the notion that the climate sensitivity of orbital forcings may be dependent on the mean climate state in agreement with Lisiecki and Raymo (2007) and Hansen et al. (2013), with possible threshold effects typical of nonlinear systems (Rial et al. 2004). Because the Plio-Pleistocene orbital forcings do not exhibit a similar increase in amplitude, it is believed that the process controlling the nonlinear behavior of the signal response originates inside the climate system. The net balance of positive and negative feedback mechanisms is the most likely process behind most of the nonlinearities in the climate (Berger and Loutre 1997; Archer et al. 2004; Rial et al. 2004; Lisiecki and Raymo 2007; Brovkin et al. 2007; Hansen et al. 2007; Hansen et al. 2011; Martinez-Boti et al. 2015).

The most important positive feedback mechanisms that are able to amplify the climate response to primary forcing are the CO_2 exchange between the ocean and the atmosphere, the water vapor feedback, the methane release from permafrost peat bogs and from hydrates, all mechanisms related to greenhouse gases, and the surface albedo feedback. Hansen et al. (2007) revealed a remarkable correspondence between the Vostok Antarctic temperature and GHG climate forcing, confirming that the temperature causes gas changes over several hundred years and suggesting that increasing warming temperature causes a net release of GHGs from oceans, soils, and the biosphere. In the EPICA ice cores, atmospheric greenhouse gases have strongly covaried with

Antarctic temperature and $\delta^{18}O$ benthic throughout eight glacial cycles over the last 800 thousand years (Jouzel et al. 2007; Luthi et al. 2008; Loulergue et al. 2008; Berger et al. 2016). Even Schneider et al. (2013) at EPICA Dome C, during the glacial inception at the end of MIS-5e, confirm a 5-kyr lag in the CO_2 decline with respect to temperatures. They explain this lag by terrestrial carbon release and carbonate compensation. Brovkin et al. (2007), by simulating the effects of changes in atmospheric and oceanic circulations in response to glacial changes in radiative forcing, find that the net effect of five feedback mechanisms related to oceanic circulation and marine biogeochemistry is able to explain a 65 ppmv drop in glacial atmospheric CO_2, compared to 80–90 ppmv recorded in the ice cores (approximately 70–80% of the total drop). Cooler oceanic water can absorb more CO_2 than warmer water. As the ocean warms, it releases CO_2 to the atmosphere, providing an amplifying climate feedback that causes further warming. If the atmosphere is warmed, the saturation vapor pressure increases, and the amount of water vapor in the atmosphere will tend to increase, leading to further warming, because water vapor is an important greenhouse gas. Liptak and Strong (2016), in a modeling study of the Arctic Sea, confirm the existence of a positive thermodynamically driven sea ice-atmosphere feedback up to 35%. A recent study shows that permafrost is a very large carbon pool stored as peat and methane in circumpolar areas (Tarnocai et al. 2009). Lawrence et al. (2008) suggest that a rapid melting of Arctic Sea ice may start a feedback loop that rapidly melts Arctic permafrost, triggering further warming feedback by the release of methane and carbon dioxide. Methane hydrates are a form of water ice saturated by a large amount of methane within its crystal structure. Extremely large deposits of methane hydrates have been found within marine sediments along continental margins of the Earth (Dickens 2003). The release of this trapped methane has the potential to cause a significant increase in temperature as a feedback mechanism triggered by bottom water warming. This hypothesis has been proposed as a possible explanation of early Cenozoic hyperthermals, such as the Paleocene-Eocene Thermal Maximum (PETM) at approximately 55 Myr, a transient warming that shows characteristics of an extreme event of short-term positive feedback (Dickens 2003; Zachos et al. 2008). If the planet becomes warmer, the ice sheet area tends to decrease, exposing a darker surface of land and open water that absorbs more sunlight, causing additional heating. Instead, during times of global cooling, additional ice increases the reflectivity, which reduces the absorption of solar radiation and results in more cooling (albedo effect). According to Hansen et al. (2013) and Hansen (2013), the net effect of fast positive feedback is to amplify the global temperature response by a factor of two to three, and this reinforcement is state dependent. Even Menviel et al. (2008) state that the atmospheric CO_2 response is a delicately balanced sum of the terrestrial and marine inventory changes, emphasizing the importance of the initial climate state on the CO_2 response to large-scale ocean circulation changes. However, exponential growth cannot continue indefinitely because some negative feedback processes act as balancing mechanisms. The new findings of Early Pliocene asymptotic decays of R_s (Fig. 11) could represent the evidence of a damping effect of carbon cycle by negative feedback processes. The continental weathering is a chemical process of atmospheric CO_2 consumption that requires tens of thousands of years to act (Walker and Hays 1981; Schrag et al. 2002; Hansen 2013). Instead, the iceberg cooling effect is a fast negative feedback that comes into play as iceberg discharge reaches a rate that cools the regional ocean surface (Hansen and Sato 2012). The interaction between vegetation and climate is another interesting component in climate system dynamics, but the question of the overall role of the biogeophysical and biogeochemical feedbacks is not yet solved because both feedbacks can be positive or negative (Claussen 2009). Nevertheless, shifts in vegetation patterns have presumably provided a negative feedback in the climate system due to their influence on carbon cycle and great areal changes. During glacial inception, forests were reduced in their areal extent leading to an increase in atmospheric CO_2 concentration, while during deglaciation, atmospheric CO_2 concentration should have decreased due to the buildup of forests (Claussen 2009). Palynological studies attest to major changes in vegetation ecosystems both at glacial and interglacial time scales (Ning et al. 1993; Elenga et al. 2000; Bertini 2010). During a glacial climate, tropical rainforests reduce in their extent to tropical seasonal forests in tropical lowlands and to xerophytic taxa in tropical highlands (Elenga et al. 2000). Boreal forests regress equatorward with a compression and fragmentation of the forest zones, while cold steppe vegetation expands (Ning et al. 1993; Bertini 2010). However, after the Zanclean and towards the Late Pleistocene, a progressive impoverishment of the subtropical forest ecosystem occurs with an increase in herbaceous taxa following the long-term cooling and drying climate trend (Ning et al. 1993; Bertini 2010). Another negative feedback mechanism is the increase in precipitation rate in a greenhouse climate that may intensify weathering rates as fresh water is flushed more rapidly through soil and sedimentary rocks (Schrag et al. 2002). Removal of CO_2 is accomplished through burial of organic carbon, and increasing river discharge may lead to a more efficient burial of organic carbon

(Schrag et al. 2002). The oceanic carbon pump by primary productivity can act as possible damping mechanism, but the complex feedback between climate and ocean require a better understanding. In fact, on orbital time scale, export production by barite accumulation rates was generally higher during cold periods (Ma et al. 2015). This interpretation could imply a positive feedback on carbon cycle that reinforces the cooler orbital response, but it is difficult to predict the net changes in CO_2 efflux (Ma et al. 2015). On the other hand, based on the long-term trends, export production was on average higher during the warmer Late Pliocene than the colder Pleistocene (Ma et al. 2015). On the contrary, the depositional conditions of the Plio-Pleistocene Mediterranean sapropels exhibit warm and wet precession-related changes of phytoplankton productivity by river runoff increasing and bottom water anoxia (Emeis 1998; Gallego-Torres et al. 2007; Moller et al. 2012), suggesting a negative feedback on carbon cycle (Schrag et al. 2002) and a possible damping effect on warming climate response.

On a geological time scale, almost all these mechanisms are sufficiently "fast" (less than 100 kyr) and can act over an orbital short-term hemicycle like precession or "semi-precession." Being geologically fast processes, the feedback response should have in theory a similar frequency modulation as the primary astronomical forcing, although the processes should exhibit a slight delay compared to the latter and to the initial temperature change induced by insolation components (Berger and Loutre 1997; Ruggieri et al. 2009; Hansen et al. 2011). The $\delta^{18}O$ and SST lags shown in the present study support this hypothesis. Moreover, the amplitude of the feedback response should be linked to the orbital hemicycle duration and to the scale effect of the surfaces/volumes involved in the processes (Schrag et al. 2002; Menviel et al. 2008; Hansen et al. 2013), a possible explanation of the nonlinear features shown in Figs. 10 and 11. Therefore, the net cumulative effect of positive and negative fast feedback mechanisms, added to the initial temperature change, could lead to the exponential response of each astronomically driven response as a function of the LT-MCS at a given time (initial condition), the duration of the orbitally paced feedback processes, and the synergy of scale-dependent processes. The different growth rates of the nonlinear orbital responses (Fig. 10) and the asymmetry in R_s (Fig. 11) suggest a high-efficiency paced system depending on whether feedbacks amplify ($R_s > 0$) or suppress ($R_s < 0$) response changes in the orbital forcings with a state-dependent magnitude related to the duration time of the feedback processes. Interestingly, the results of the present study indicate an amplified orbital response during times of a global icehouse state (Mid-Late Pleistocene, with the remarkable exception of obliquity), which can reach a magnitude of three to five times global $\delta^{18}O$ or two to three times tropical SST forcing, and a maximum of two times the damped response for all signals during the time of a global greenhouse state (Early Pliocene). In this study, it is proposed that orbital response be considered basically as composite feedback responses paced by orbital and damped or amplified in a range of − 100 to + 400% the forcing, as function of the LT-MCS at a given time (initial conditions), the hemicycle duration, and the synergy of the feedback processes. Therefore, the sensitivity of the climate system to orbital forcings could depend on the long-term climate factors in terms of average atmospheric GHG composition, the average concentration of volcanic aerosols, the global mean temperature, the cryosphere average volume, and, presumably, the global forest cover and ocean primary productivity, factors affecting high-efficiency feedback mechanisms related to carbon cycle and ice-albedo. This interpretation may explain the energy excess "paradox" of the astronomically paced signals compared to the small energy of the orbital forcing, especially concerning the eccentricity bands (Imbrie et al. 1993; Wunsch 2004; Berger et al. 2005; Berger et al. 2012). The progressive increase in the strength of the 95-kyr $\delta^{18}O$ response from the Zanclean (very weak) to the Mid-Late Pleistocene may be interpreted as the effect of increased sensitivity to eccentricity due to the growing trend of the global ice volume following the cooling trend. In this time interval, the LT-LR04 component undergoes an average enrichment from 2.99‰ (Zanclean) to 4.18‰ (Middle Pleistocene-Holocene) due to long-term changes in atmosphere composition, and the climate system may become sensitive to the weak eccentricity insolation by overcoming the critical condition of global mean temperature and average ice volume, a hypothesis already formulated by Raymo (1998) and many others (Berger et al. 1999; Raymo et al. 2006; Berger and Yin 2012). The models of Imbrie et al. (2011) and Abe-Ouchi et al. (2013) also support this hypothesis. Their studies show that ice volume plays a very important role in pacing the orbital response of the climate system. Considering orbital signals basically as feedback responses paced by orbitals may explain why the ~ 100-kyr eccentricity-driven response is so strong post-MPT, when the obliquity "ice killing," which prevents a long-life ice sheet, was strongly mitigated by damping effect (Fig. 11). Also, the hysteresis loop of the North American ice sheet may have contributed to lead a long-life ice sheet. After the inception of the ice sheet, its mass balance remains mostly positive through several precession cycles, whose amplitudes decrease towards an eccentricity minimum (Abe-Ouchi et al. 2013). The larger the ice sheet grows and extends towards lower latitudes, the smaller is the insolation required to make the mass

balance negative. A long-life ice sheet sensitive to eccentricity during a time of a global icy state may have activated a synergistic response of positive feedback processes modulated on ~ 100-kyr eccentricity response times. The negligible response of $\delta^{18}O$ in the eccentricity band during the Zanclean could be due to the higher mean temperature and the lower mean global ice volume, which would fail to move permanently to the climate signal due to obliquity "ice killing," a powerful forcing during this period. Considering the asymptotic decay of the $\delta^{18}O$ and SST R_s up to a maximum of − 100% towards the Early Pliocene (Fig. 11), a working hypothesis could be a damping effect due to the action of negative feedbacks during the time of higher global average temperature, such as, for instance, a higher global forest coverage, a greatest ocean primary productivity, and a more efficient burial of organic carbon. Zanclean was a period of global greenhouse state, characterized by high atmospheric GHGs and mean global temperature (Bertini 2010; Seki et al. 2010; Bartoli et al. 2011). During Zanclean, northern and central Italy were covered by vegetation dominated by hygrophilous and thermophilous forest taxa typical of a humid subtropical to warm-temperate climate. Precipitation was sufficiently high for the persistence of a "broad-leaved evergreen/warm temperate mixed forest" up to 3.5 Myr (Bertini 2010). Therefore, a wide forest cover, along with a possible high ocean primary productivity and organic carbon burial, could increase the quantitative role of the CO_2-related negative feedbacks (Emeis 1998; Schrag et al. 2002; Gallego-Torres et al. 2007; Claussen 2009; Moller et al. 2012; Ma et al. 2015) causing a damping effect of the orbitally paced responses. In the Mid-Late Pleistocene, an icy state leads to a significant reduction in global forest cover, making these processes quantitatively less important but emphasizing the vegetation-snow albedo feedback in synergy with the sea-ice albedo feedback which tends to amplify Northern Hemisphere and global mean temperature changes (Claussen 2009).

Mid-Late Pleistocene obliquity damped responses

To attempt the interpretation of these nonlinear features (Figs. 10 and 11), some possible mechanisms are discussed in this section as working hypotheses for future studies. The global $\delta^{18}O$ and tropical SST sharply decline to near-zero in obliquity R_s during the Mid-Late Pleistocene suggesting an attenuation mechanism of the obliquity driving force and, consequently, a reduction of the feedback amplification processes linked to the mean icy state. Understanding this phenomenon is important because the post-MPT obliquity forcing attenuation could have contributed to the strengthening of the eccentricity response, favoring a long-life ice growth. Lisiecki and Raymo (2007) state that the change in $\delta^{18}O$ glacial dynamics at ~ 1.4 Myr is associated with an abrupt decline in 41-kyr power and a decrease in modulation sensitivity to obliquity. Interestingly, the shape of the $\delta^{18}O$ and SST components-3-4 after the MPT (Figs. 4c and 8c), characterized by the envelope of two to three low-amplitude obliquity cycles in a weak ~ 90–93-kyr framework, suggests a connection between eccentricity and obliquity, similar to that proposed by Huybers (2007) of obliquity-cycle skipping. The obliquity-pacing results indicate that the 100-kyr variability could result from the skipping of one or two obliquity beats, corresponding to 80-kyr or 120-kyr glacial cycles that, on average, give 100-kyr periodicity, resulting from long-term changes in the climate system, such as ice sheet growth (Huybers 2007). Why does obliquity-cycle skipping occur? Climate friction is a dissipative feedback between obliquity variations and climate which may cause a secular drift of the spin axis (Laskar et al. 2004). In response to obliquity forcing, glacial and interglacial conditions drive the redistribution of the ice/water mass and the isostatic adjustment to the surface loading, affecting the dynamical ellipticity of the Earth (obliquity–oblateness feedback) (Rubincam 1993, 1995; Levrard and Laskar 2003; Laskar et al. 2004). Delayed responses in both climatic and viscous relaxation processes may introduce a secular term in the obliquity evolution (Rubincam 1995). Because both the Earth's ice load history and viscoelastic structure are not strongly constrained, it is difficult to produce accurate predictions of the coupled response of the entire system (Laskar et al. 2004). Therefore, simplifying assumptions have to be made to estimate the magnitude and the direction of the secular drift (increase or decrease in the obliquity). Specifically, the sign of the secular obliquity change is particularly sensitive to the obliquity-lag estimates and changes of oblateness (Williams et al. 1998; Levrard and Laskar 2003). Levrard and Laskar (2003) showed that climate friction impact is positive and likely negligible over the last 3 Myr, based on the model assumptions that the ice sheet response time-lag could not be longer than the obliquity period and explicitly assumed it to be 8 kyr. However, the secular change of obliquity becomes negative for low obliquity lag response (< 4.2 kyr) and high positive change of oblateness (Levrard and Laskar 2003). Response lags are difficult to estimate. According to Lisiecki and Raymo (2005a), the $\delta^{18}O$ lag in obliquity reaches values of ~ 6.8 kyr in the Pleistocene. The results of the present study indicate a $\delta^{18}O$ obliquity lag of 7.4 kyr post-MPT (Table 8), close to the value used by Levrard and Laskar (2003). In contrast, the obliquity lag estimation of Hilgen et al. (1993) provides a lower value of 5.6 kyr with respect to the Late Pleistocene if the phase relation with precession is kept constant. Considering the margin of error of these estimates, it is currently not possible to establish whether the obliquity lags may be lower post-MPT to justify the observed obliquity damping effect. Furthermore,

other simplified assumptions in the dissipative equations model, together with age model bias, could affect the final results. A recent study by Adhikari and Ivins (2016) using space geodetic and satellite gravimetric present-day data has shown that global-scale continent-ocean mass transport changes (terrestrial water storage and global cryosphere) explain nearly the entire amplitude (83 ± 23%) and mean directional shift (within 5.9° ± 7.6°) of the observed polar motion on a very short present-day time scale. The study of Adhikari and Ivins (2016) suggests a high sensitivity of the poles to the mass transport changes and to the isostatic rebound. In conclusion, new studies are needed to clarify the effective role of climate friction or to identify other mechanisms that might be responsible for this unusual transition in obliquity response.

Tropical SST coupled with benthic $\delta^{18}O$ cycles

Despite the differences in signal-to-noise ratio and oceanographic context between the LR04 $\delta^{18}O$ and the ODP Site 846 SST records (global benthic stack and upwelling tropical single record), the SSA results show the tropical SST tightly coupled with benthic $\delta^{18}O$ over the past five million years, both at long and orbital time scales, in agreement with the original work of Herbert et al. (2010a). Some differences certainly exist (e.g., a strong cooling event at ~ 2.1 kyr or MBO warming less marked in the SST signal; the tropical trend cooling slightly negative shifted compared to global ΔSST, nonetheless subparallel in time) (Fig. 14b), but they may be explained in terms of temporal and regional upwelling effects at the ODP Site 846. These similarities suggest common causes for both the $\delta^{18}O$ long-term trend and cycles and their expression in the tropical SST. The most likely candidate for some orbitally paced cycles lies in high-latitude oceanographic processes tied to the global carbon cycle (Liu and Herbert 2004; Herbert et al. 2010a). These processes drive the oceanic circulation through changes in deep water properties, affecting vertical density stability and upwelling in the tropical oceans. Changes in the atmospheric GHG composition controlled by insolation processes in the high latitudes may also act to imprint obliquity on the tropical Pacific where the local direct effect of obliquity is weak (Liu and Herbert 2004; Medina-Elizalde and Lea 2005; Masson-Delmotte et al. 2006). The $\delta^{18}O$-SST delta-lag in obliquity became large after the beginning of the MPT, suggesting a signal of global ice volume growth (Table 8). Such observations, together with the high coherence between SST and $\delta^{18}O$ obliquity responses (Table 9) may suggest remote connections from high latitudes towards the tropics. These interpretations could explain why the tropical SST obliquity component contains a small variance in comparison to that of $\delta^{18}O$ (5.5% vs. 9.9%). The smaller coherency between tropical SST and $\delta^{18}O$ precession components (Table 9) might indicate that the response in the EEP was caused by low-latitude precession forcing and regional effects and was less coupled to the high-latitude ice volume (Liu and Herbert 2004). Tachikawa et al. (2014) found residual SST variability characterized by a 23-kyr periodicity in the western Pacific warm pool (WPWP) region. They concluded a wind-driven northward surface current advection towards the WPWP to be responsible for the regional SST precessional periodicity, attributed to meridional shifts of the Intertropical Convergence Zone. Even the "half-precession" cycle of equatorial origin (Berger et al. 2006), isolated in this study by SSA from both tropical SST and global $\delta^{18}O$ records, may be transmitted to high latitudes via advective transport (Hagelberg et al. 1994). The last interglacial half-precession cycle from the Northwestern Chinese Loess Plateau, interpreted as a direct response to low-latitude forcing through its modulation on the East Asian summer monsoon (Sun and Huang 2006), supports this interpretation. The coherency increase of the short eccentricity's $\delta^{18}O$ and SST signals and the maximum delta-lag in eccentricity between $\delta^{18}O$ and SST (4.31 vs. 0.44 kyr) towards the Late Pleistocene (Table 8) may reflect the progressive rise of eccentricity power and an increased contribution of the high-latitude $\delta^{18}O$ ice volume component over the water temperature signal. Berger et al. (2006) show the presence of significant 100-kyr and 11-kyr cycles in the amplitude of the seasonal cycle in the intertropical regions, but the amplitude decreases rapidly when moving away from the equator. The small differences in variance between the short eccentricity's SST and $\delta^{18}O$ components (5.1% vs. 6.5%) might depend on these considerations. Conversely, the big difference in variance of the closely enveloped long-term cycles (Earth's orbit secular frequencies, obliquity modulation cycles, and long eccentricity cycles) between SST (10.3%) and $\delta^{18}O$ (4.2%) components could suggest a greater sensitivity of the tropics to these long-term cycles. The tropical oceans should be shielded from feedback processes that produce large temperature sensitivity in the high latitudes, such as ice-albedo feedbacks, sea ice-atmosphere feedback, and permafrost feedback (Lawrence et al. 2008; Tarnocai et al. 2009; Herbert et al. 2010a; Liptak and Strong 2016). With the exception of obliquity, the marked difference in eccentricity and precession R_s in the Late Pleistocene between $\delta^{18}O$ (200–400%) and SST (100–170%) (Fig. 11) may be due to a lower synergy of the positive feedback mechanisms in tropical regions. In summary, both remote connections from high-latitude and direct low-latitude orbital forcings could couple Plio-Pleistocene global $\delta^{18}O$ and tropical SST orbital cycles through oceanic and atmospheric circulations. Finally, the remarkable constancy (~ 76%) of the Plio-Pleistocene trend variance among global $\delta^{18}O$, local tropical SST (Site 846), and global SST (ΔSST stack) might reflect the

latitude-independent nature of the long-term factors controlling the atmosphere composition and global mean temperature.

Conclusions

The main conclusions of this study can be summarized as follows:

1) A detailed evaluation is provided of the variance paced by long-period orbital modulation, short eccentricity, obliquity, precession, and half-precession cycles, estimated for the $\delta^{18}O$ at approximately 4.2%, 6.5%, 9.9%, 2.0%, and 0.6%, respectively, and for the tropical SST at about 10.3%, 5.1%, 5.5%, 1.6%, and 0.5%, respectively, both resulting in total orbital contributions of ~ 23.0%. On long time scales, the Plio-Pleistocene astronomical forcing could be considered a random walk at zero-sum in which the orbital responses oscillate around a basically time-invariant quasi-normal distributed mean, supporting the hypothesis that orbital forcings did not have a major role in guiding the Plio-Pleistocene climate system response.
2) The exponential growth of the orbital variance towards the Late Pleistocene is function of the LT-MCS at a given time and regards all $\delta^{18}O$ and SST components with an increasing rate related to the orbital period, from half-precession to eccentricity. The asymmetry of the R_s suggests an amplified orbital response during times of a global icehouse state (Mid-Late Pleistocene, with the exception of obliquity), which can reach a magnitude of + 200 to + 400% global $\delta^{18}O$ forcing, or + 100 to + 170% the tropical SST forcing, and a minimum up to − 100% the damped response for all signals during time of a global greenhouse state (Early Pliocene).
3) It is proposed that orbital responses be considered as composite feedback lagged responses paced by orbitals and damped or amplified in a range of − 100 to + 400% the forcing, depending on the initial conditions set by LT-MCS, the hemicycle duration, and the synergy of the feedback processes related to carbon cycles and albedo effects. This interpretation may explain the energy excess "paradox" of the astronomically paced signals compared to the small energy of the orbital forcing, especially concerning the eccentricity bands.
4) The asymptotic decay of the $\delta^{18}O$ and SST R_s up to − 100% towards the Early Pliocene could be due to a damping effect of negative feedbacks during a time of higher mean global temperature. Zanclean was a period of global greenhouse state, and a wide forest cover along with a possible high ocean primary productivity and a more efficient burial of organic carbon could have increased the quantitative role of the CO_2-related negative feedbacks, causing a damping effect of the orbitally paced responses.
5) The global $\delta^{18}O$ and tropical SST anomalous sharply decline to near-zero in obliquity R_s during the Late Pleistocene suggesting an attenuation mechanism of the obliquity driving force and a reduction of the related feedback amplification processes. The post-MPT obliquity damping may have contributed to the strengthening of the eccentricity response by mitigating the obliquity "ice killing," favoring a 100-kyr long-life hysteresis ice growth volume. A long-life ice sheet sensitive to eccentricity during the time of a global icy state may have activated a synergistic response of positive feedback processes modulated on short eccentricity response times. In the Mid-Late Pleistocene, an icy state leads to a significant reduction in global forest cover making its negative feedbacks quantitatively less important but emphasizing the positive feedback processes, such as the vegetation-snow albedo in synergy with the sea-ice albedo and permafrost feedbacks. However, the origin of the post-MPT obliquity attenuation mechanism is an open question.
6) The tropical SST orbital cycles are tightly coupled with the global benthic $\delta^{18}O$ cycles over the past five million years, suggesting both Plio-Pleistocene oceanic and atmospheric remote connections from high-latitude and direct low-latitude orbital forcings.
7) The tropical SST, the global SST, and the global $\delta^{18}O$ trend components, each explaining ~ 76% of the Plio-Pleistocene climate variance, could be related to the long-term pCO_2 proxies, suggesting non-orbital latitude-independent control factors. These trend components significantly change the climate mean using arbitrary time intervals, suggesting the Plio-Pleistocene mean climate state was changed primarily by long-term carbon cycle controlling the Earth's atmospheric composition. The geotectonic forcing appears to be a plausible hypothesis to explain the long-term changes in atmospheric composition (GHGs and volcanic aerosols) through direct (CO_2 outgassing and explosive volcanism) and indirect (orography and erosion, paleogeography, oceanic paleocirculation, and ocean fertilization) control by plate tectonics.
8) The NHG gradually developed in four phases (subtrends) of progressive lowering of the average temperatures and ice volume growth, triggered by long-term changes in the atmospheric composition. Nevertheless, transient interaction effects with very long-term orbital cycles, expression of the chaotic behavior of the solar system, may have contributed

to setting these transitions. After MIS-16, the cooling trend was broken by a wide swing of $\delta^{18}O$ depletion and SST recovery, a relative stasis of ice growth and temperature cooling during the last 600 kyr (MBO), which could be related to mid-term GHG recovery.

The idea of the geotectonic forcing is the most attractive hypothesis by a long time, and the recent improvements in the seafloor spreading rate evaluation lead in the right direction. However, further studies are needed to better estimate high-resolution seafloor spreading rate and to assess the role of the volcanic CO_2 degassing and the explosive volcanic aerosols in the budget of the carbon cycle. Even much higher resolution CO_2 proxies, covering a long time period, are necessary to better address carbon cycle. Nevertheless, the relevance of the primary long-term climate system, controlling the Earth's atmospheric composition and modifying the average global climate, must be underlined. Finally, singular spectrum analysis provides a valuable tool in cyclostratigraphy with the remarkable advantage of separating full-resolution time series by variance strength.

Additional files

Additional file 1: Methodology. (DOC 1687 kb)
Additional file 2: Dataset. (XLS 3816 kb)
Additional file 3: High-resolution figures. (PDF 6502 kb)

Abbreviations

ANOVA: Analysis of variance; EECO: Early Eocene Climatic Optimum; EEP: Eastern Equatorial Pacific; EPICA: European Project for Ice Coring in Antarctica; FFS: Fourier frequency spectrum; FFT: Fast Fourier transform; GASR: Global average spreading rate; GCM: General circulation model; GHG: Greenhouse gas; GSSP: Global Stratotype Section and Point; HT846: Herbert et al. (2010b) sea surface temperature of ODP Site 846; INHG: Intensification of Northern Hemisphere Glaciation; LGM: Last Glacial Maximum; LIP: Large igneous province; LT-HT846: Long-term HT846 SST component; LT-LR04: Long-term LR04 $\delta^{18}O$ component; LT-MCS: Long-term mean climate state; MBE: Mid-Brunhes Event; MBO: Mid-Brunhes Oscillation; MIS: Marine Isotope Stage; MMCO: Middle Miocene Climatic Optimum; MPT: Mid-Pleistocene Transition; NASSR: North Atlantic seafloor spreading rate; NHG: Northern Hemisphere Glaciation; ODP: Ocean Drilling Program; ONHG: Onset of the Northern Hemisphere Glaciation; PETM: Paleocene-Eocene Thermal Maximum; R_s: Response sensitivity; SSA: Singular spectrum analysis; SST: Sea surface temperature; TISA: Time-integral squared amplitude; WPWP: Western Pacific warm pool

Acknowledgements

Special thanks to Gian Battista Vai for the useful suggestions and for the encouragement to publish the study. I am grateful to Francesco Mulargia for the methodological review. Thanks also to Nicola Scafetta for the useful discussion. I thank Lorraine Lisiecki for kindly providing me the $\delta^{13}C$-based pCO_2 proxy data. Special thanks to Alessandra Negri for improving the English language and other constructive comments.

Funding

This research did not receive any specific grant from funding agencies in the public, commercial, or not-for-profit sectors.

Availability of data and materials

Details on the methodology used in this study and a discussion of the quality and reliability of the time series can be found in Additional file 1. The complete SSA-components dataset and a complete set of high-resolution figures are also provided:

- Additional file 1 - Methodology.doc
- Additional file 2 - Dataset.xls
- Additional file 3 - High resolution figures.pdf

Authors' contributions

The author read and approved the final manuscript.

Competing interests

The author declares that he has no competing interests.

Publisher's Note

Received: 16 April 2018 Accepted: 29 October 2018
Published online: 07 December 2018

References

Abe-Ouchi A, Saito F, Kawamura K, Raymo ME, Okuno J, Takahashi K, Blatter H (2013) Insolation-driven 100,000-year glacial cycles and hysteresis of ice-sheet volume. Nature 500. https://doi.org/10.1038/nature12374

Adhikari S, Ivins ER (2016) Climate-driven polar motion: 2003–2015. Sci Adv 2. https://doi.org/10.1126/sciadv.1501693

Aitchison JC, Ali JR, Davis AM (2007) When and where did India and Asia collide? J Geophys Res 112:B05423. https://doi.org/10.1029/2006JB004706

Archer D, Martin P, Buffett B, Brovkin V, Rahmstorf S, Ganopolski A (2004) The importance of ocean temperature to global biogeochemistry. Earth Planet Sci Lett 222(2004):333–348. https://doi.org/10.1016/j.epsl.2004.03.011

Bartoli G, Hönisch B, Zeebe RE (2011) Atmospheric CO2 decline during the Pliocene intensification of northern hemisphere glaciations. Paleoceanography 26:PA4213. https://doi.org/10.1029/2010PA002055

Bartoli G, Sarnthein M, Weinelt M, Erlenkeuser H, Garbe-Schonberg D, Lea DW (2005) Final closure of Panama and the onset of northern hemisphere glaciation. Earth Planet Sci Lett 237(2005):33–44. https://doi.org/10.1016/j.epsl.2005.06.020

Becker TW, Conrad CP, Buffett B, Dietmar MR (2009) Past and present seafloor age distributions and the temporal evolution of plate tectonic heat transport. Earth Planet Sci Lett 278(2009):233–242. https://doi.org/10.1016/j.epsl.2008.12.007

Beerling DJ, Royer DL (2011) Convergent Cenozoic CO_2 history. Nat Geosci 4, pp. 418-420.

Berger A, Li XS, Loutre MF (1999) Modelling northern hemisphere ice volume over the last 3 Myr. Quat Sci Rev 18(1999):1–11

Berger A, Loutre MF (1997) Long-term variations in insolation and their effects on climate, the LLN experiments. Surv Geophys 18:147–161

Berger A, Loutre MF, Mélice JL (2006) Equatorial insolation: from precession harmonics to eccentricity frequencies. Clim Past Discuss 2:519–533 https://doi.org/10.5194/cp-2-131-2006

Berger A, Mélice JL, Loutre MF (2005) On the origin of the 100-kyr cycles in the astronomical forcing, Paleoceanography, 20:PA4019, https://doi.org/10.1029/2005PA001173.

Berger A, Yin Q (2012) Modeling the interglacials of the last 1 million years. In: Berger et al (eds) Climate change: inferences from paleoclimate and regional aspects. Springer-Verlag, Wien 2012.

Berger A, Yin QZ, Herold N (2012) MIS-11 and MIS-19, analogs of our Holocene interglacial. In: 3rd International Conference on Earth System Modelling, Hamburg, https://meetingorganizer.copernicus.org/3ICESM/3ICESM-11.pdf

Berger A et al (2016) Past interglacials working group of PAGES, interglacials of the last 800,000 years. Rev Geophys 54:162–219. https://doi.org/10.1002/2015RG000482

Berger AL (1978) Long-term variations of daily insolation and quaternary climatic change. J Atmos Sci 35:2362–2367

Berner RA, Kothavala Z (2001) GEOCARB III: a revised model of atmospheric CO_2 over phanerozoic time. Am J Sci 301(2):182–204

Berner RA, Lasaga AC, Garrels RM (1983) The carbonate-silicate geochemical cycle and its effect on atmospheric carbon dioxide over the past 100 million years. Am J Sci 283:641–683

Bertini A (2010) Pliocene to Pleistocene palynoflora and vegetation in Italy - state of the art. Quat Int 225(2010):5–24

Blanc PL, Fontugne MR, Duplessy JC (1983) The time-transgressive initiation of boreal ice-cap: continental and oceanic evidence reconciled. Palaeogeogr Palaeoclimatol Palaeoecol 42:211–224

Boulila S, Galbrun B, Miller KG, Pekar SF, Browning JV, Laskar J, Wright JD (2011) On the origin of Cenozoic and Mesozoic "third-order" eustatic sequences. Earth Sci Rev 109:94–112

Brady PV, Gislason SR (1997) Seafloor weathering controls on atmospheric CO_2 and global climate. Geochimica Et Cosmochimica Acta 61(5):965–973

Brovkin V, Ganopolski A, Archer D, Rahmstorf S (2007) Lowering of glacial atmospheric CO2 in response to changes in oceanic circulation and marine biogeochemistry. Paleoceanography 22:PA4202. https://doi.org/10.1029/2006PA001380

Clark PU, Archer D, Pollard D, Blum JD, Rial JA, Brovkin V, Mix AC, Pisias NG, Roy M (2006) The middle Pleistocene transition: characteristics, mechanisms, and implications for long-term changes in atmospheric pCO2. Quat Sci Rev. https://doi.org/10.1016/j.quascirev.2006.07.008

Claussen M (2009) Late Quaternary vegetation-climate feedbacks. Clim Past 5: 203–216, https://doi.org/10.5194/cp-5-203-2009

Cogné JP, Humler E (2006) Trends and rhythms in global seafloor generation rate. Geochem Geophys Geosyst 7:Q03011. https://doi.org/10.1029/2005GC001148

Coltice N, Seton M, Rolf T, Müller RD, Tackley PJ (2013) Convergence of tectonic reconstructions and mantle convection models for significant fluctuations in seafloor spreading. Earth Planet Sci Lett 383(2013):92–100. https://doi.org/10.1016/j.epsl.2013.09.032

Conrad CP, Lithgow-Bertelloni C (2007) Faster seafloor spreading and lithosphere production during the mid-Cenozoic. Geology 35(1):29–32. https://doi.org/10.1130/G22759A

Dickens GR (2003) Rethinking the global carbon cycle with a large, dynamic and microbially mediated gas hydrate capacitor. Earth Planet Sci Lett 213(2003):169–183. https://doi.org/10.1016/S0012-821X(03)00325-X

Elenga H et al (2000) Pollen-based biome reconstruction for southern Europe and Africa 18,000 years ago. J Biogeogr 27:621–634

Elsner JB, Tsonis AA (1996) Singular spectrum analysis: a new tool in time series analysis. Springer

Emeis K.-C., Sakamoto T. (1998) - The Sapropel Theme of Leg 160. In: Robertson A.H.F., Emeis K.-C., Richter C. & Camerlenghi A. (Eds.). Proceedings of the ocean drilling program, scientific results. 160

Gallego-Torres D, Martínez-Ruiz F, Paytan A, Jiménez-Espejo FJ, Ortega-Huertas M (2007) Pliocene–Holocene evolution of depositional conditions in the eastern Mediterranean: role of anoxia vs. productivity at time of sapropel deposition. Palaeogeogr Palaeoclimatol Palaeoecol 246(2007):424–439. https://doi.org/10.1016/j.palaeo.2006.10.008

Ghil M, Allen RM, Dettinger MD, Ide K, Kondrashov D, Mann ME, Robertson A, Saunders A, Tian Y, Varadi F, Yiou P (2002) Advanced spectral methods for climatic time series. Rev Geophys 40(1):3.1–3.41. https://doi.org/10.1029/2001RG000092

Gibbard PL, Head MJ (2009) IUGS ratification of the Quaternary system/period and the Pleistocene series/epoch with a base at 2.58 Myr. Quaternaire 20(4):411–412

Hagelberg TK, Bond G, deMenocal P (1994) Milankovitch band forcing of sub-Milankovitch climate variability during the Pleistocene. Paleoceanography 9(4):545–558. https://doi.org/10.1029/94PA00443

Hansen J. (2013) - An old story, but useful lessons. http://www.columbia.edu/~jeh1/mailings/2013/20130926_PTRSpaperDiscussion.pdf

Hansen J, Sato M (2012) Paleoclimate implications for human-made climate change. In: Berger A, Mesinger F, Sijacki D (eds) Climate change. Inferences from paleoclimate and regional aspects. Springer-Verlag, Wien 2012, p 350, https://doi.org/10.1007/978-3-7091-0973-1_2

Hansen J, Sato M, Kharecha P, Russell G, Lea DW, Siddall M (2007) Climate change and trace gases. Phil Trans R Soc A 365:1925–1954. https://doi.org/10.1098/rsta.2007.2052

Hansen J, Sato M, Kharecha P, von Schuckmann K (2011) Earth's energy imbalance and implications. Atmos Chem Phys 11:13421–13449, https://doi.org/10.5194/acp-11-13421-2011

Hansen J, Sato M, Russell G, Kharecha P (2013) Climate sensitivity, sea level and atmospheric carbon dioxide. Phil Trans R Soc A 371:20120294. https://doi.org/10.1098/rsta.2012.0294

Hansen et al (2005) Efficacy of climate forcings. J Geophys Res 110:D18104. https://doi.org/10.1029/2005JD005776

Hassani H (2007) Singular spectrum analysis: methodology and comparison. J Data Sci 5(2007):239–257

Head M.J. & Gibbard P.L. (2005) - Early–Middle Pleistocene transitions. An overview and recommendation for the defining boundary. From: Head MJ & Gibbard PL (eds). Early–middle Pleistocene transitions: the land–ocean evidence. Geological Society, London, Special Publications, 247, 1–18. 0305–8719/05/$15© The Geological Society of London 2005

Head MJ, Pillans B, Farquhar SA (2008) The Early–Middle Pleistocene transition: characterization and proposed guide for the defining boundary. Episodes 31(2):255–259

Herbert TD, Peterson LC, Lawrence KT, Liu Z (2010a) Tropical ocean temperatures over the past 3.5 million years. Science 328:1530–1534. https://doi.org/10.1126/science.1185435

Herbert T.D., Peterson L.C., Lawrence K.T. & Liu Z. (2010b) - Plio-Pleistocene tropical alkenone SST reconstructions LAST UPDATE: 6/2010, NOAA/NCDC Paleoclimatology Program. ftp://ftp.ncdc.noaa.gov/pub/data/paleo/contributions_by_author/herbert2010/herbert2010.txt

Hilgen FJ, Lourens LJ, Berger A, Loutre MF (1993) Evaluation of the astronomically calibrated time scale for the Late Piocene and the earliest Pleistocene. Paleoceanography 8:549–565

Hönisch B, Hemming NG, Archer D, Siddall M, McManus JF (2009) Atmospheric carbon dioxide concentration across the mid-Pleistocene transition. Science 324:1551. https://doi.org/10.1126/science.1171477

Huybers P (2007) Glacial variability over the last two million years: an extended depth-derived agemodel, continuous obliquity pacing, and the Pleistocene progression. Quat Sci Rev 26(2007):37–55

Imbrie J, Berger A, Boyle EA, Clemens SC, Duffy A, Howard WR, Kukla G, Kutzbach J, Martinson DG, Mcintyre A, Mix AC, Molfino B, Morley JJ, Peterson LC, Pisias NG, Prell WL, Raymo ME, Shackleton NJ, Toggweile JR (1993) On the structure and origin of major glaciation cycles 2. The 100,000-year cycle. Paleoceanography 8(6):699–735

Imbrie JZ, Imbrie-Moore A, Lisiecki LE (2011) A phase-space model for Pleistocene ice volume. Earth Planet Sci Lett 307:94–102

Jicha BR, Scholl DW, Rea DK (2009) Circum-Pacific arc flare-ups and global cooling near the Eocene Oligocene boundary. Geology 37(4):303–306. https://doi.org/10.1130/G25392A.1

Jouzel J et al (2007) Orbital and millennial Antarctic climate variability over the past 800,000 years. Science 317:793–796. https://doi.org/10.1126/science.1141038

Joyce JE, Tjalsma LRC, Prutzman JM (1990) High-resolution planktic stable isotope record and spectral analysis for the last 5.35 M.Y.: Ocean Drilling Program site 625 northeast Gulf of Mexico. Paleoceanography 5:507–529

Kent DV, Muttoni G (2013) Modulation of Late Cretaceous and Cenozoic climate by variable drawdown of atmospheric pCO_2 from weathering of basaltic provinces on continents drifting through the equatorial humid belt. Clim Past 9:525–546. https://doi.org/10.5194/cp-9-525-2013

Kominz M, Pisias N (1979) Pleistocene climate: deterministic or stochastic? Science 204(Issue 4389):171–173. https://doi.org/10.1126/science.204.4389.171

Laskar J, Fienga A, Gastineau M, Manche H (2011) La2010: a new orbital solution for the long-term motion of the Earth. Astron Astrophys 532:A89. https://doi.org/10.1051/0004-6361/201116836

Laskar J, Joutel F, Boudin F (1993) Orbital, precessional and insolation quantities for the Earth from −20 Myr to +10 Myr. Astron Astrophys 270:522–533

Laskar J, Robutel P, Joutel F, Gastineau M, Correia ACM, Levrard B (2004) A long term numerical solution for the insolation quantities of the Earth. Astron Astrophys 428:La2004

Lawrence DM, Slater AG, Tomas RA, Holland MM, Deser C (2008) Accelerated Arctic land warming and permafrost degradation during rapid sea ice loss. Geophys Res Lett 35:L11506. https://doi.org/10.1029/2008GL033985

Le Breton E, Cobbold PR, Dauteuil O, Lewis G (2012) Variations in amount and direction of seafloor spreading along the Northeast Atlantic Ocean and resulting deformation of the continental margin of Northwest Europe. Tectonics 31:TC5006. https://doi.org/10.1029/2011TC003087

Levrard B, Laskar J (2003) Climate friction and the Earth's obliquity. Geophys J Int 154:970–990

Li G, Elderfield H (2013) Evolution of carbon cycle over the past 100 million years. Geochim Cosmochim Acta 103(2013):11–25. https://doi.org/10.1016/j.gca.2012.10.014

Liptak J, Strong C (2016) A modeling investigation of the Arctic Sea ice-atmosphere feedback. Clim Dyn 47(Issue 7):2471–2480

Lisiecki LE (2010a) Links between eccentricity forcing and the 100,000-year glacial cycle. Nat Geosci 3. https://doi.org/10.1038/NGEO828

Lisiecki LE (2010b) A benthic $\delta^{13}C$-based proxy for atmospheric pCO_2 over the last 1.5 Myr. Geophys Res Lett 37:L21708. https://doi.org/10.1029/2010GL045109

Lisiecki LE, Raymo ME (2005a) A Pliocene-Pleistocene stack of 57 globally distributed benthic δ18O records. Paleoceanography 20:PA1003. https://doi.org/10.1029/2004PA001071

Lisiecki L.E. & Raymo M.E. (2005b) Appendix 1 - Global Plio-Pleistocene stack of benthic oxygen isotope records. DOI:https://doi.org/10.1594/PANGAEA.701576. DOI:https://doi.org/10.1029/2004PA001071. In supplement to: Lisiecki & Raymo (2005)

Lisiecki LE, Raymo ME (2007) Plio–Pleistocene climate evolution; trends and transitions in glacial cycle dynamics. Quat Sci Rev 26(2007):56–69. https://doi.org/10.1016/j.quascirev.2006.09.005

Liu Z, Herbert TD (2004) High-latitude influence on the eastern equatorial Pacific climate in the early Pleistocene epoch. Nature 427:720–723

Lo L, Chang S, Wei K, Lee S, Ou T, Chen Y, Chuang C, Mii H, Burr GS, Chen M, Tung Y, Tsai M, Hodell DA, Shen C (2017) Nonlinear climatic sensitivity to greenhouse gases over past 4 glacial/interglacial cycles. Nat Sci Rep 7:4626. https://doi.org/10.1038/s41598-017-04031-x

Loulergue L, Schilt A, Spahni R, Masson-Delmotte V, Blunier T, Lemieux B, Barnola JM, Raynaud D, Stocker TF, Chappellaz J (2008) Orbital and millennial-scale features of atmospheric CH4 over the past 800,000 years. Nature 453. https://doi.org/10.1038/nature06950

Lourens LJ, Hilgen FJ (1994) Long-period orbital variations and their relation to third-order eustatic cycles and the onset of major glaciations 3.0 million years ago. In: Lourens LJ (ed) Astronomical forcing of Mediterranean climate during the last 5.3 million years. Thesis Utrecht University, ISBN 90-393-0754-7

Lunt DJ, Foster GL, Haywood AM, Stone EJ (2008) Late Pliocene Greenland glaciation controlled by a decline in atmospheric CO_2 levels. Nature 454:1102–1106. https://doi.org/10.1038/nature07223

Lunt DJ, Haywood AM, Schmidt GA, Salzmann U, Valdes PJ, Dowsett HJ, Loptson CA (2012) On the causes of mid-Pliocene warmth and polar amplification. Earth Planet Sci Lett 321-322(2012):128–138. https://doi.org/10.1016/j.epsl.2011.12.042

Luthi D, Le Floch M, Bereiter B, Blunier T, Barnola JM, Siegenthaler U, Raynaud D, Jouzel J, Fischer H, Kawamura K, Stocker TF (2008) High-resolution carbon dioxide concentration record 650,000–800,000 years before present. Nature 453. https://doi.org/10.1038/nature06949

Ma Z, Ravelo AC, Liu Z, Zhou L, Paytan A (2015) Export production fluctuations in the eastern equatorial Pacific during the Pliocene-Pleistocene: reconstruction using barite accumulation rates. Paleoceanography 30. https://doi.org/10.1002/2015PA002860

Martinez-Boti MA, Foster GL, Chalk TB, Rohling EJ, Sexton PF, Lunt DJ, Pancost RD, Badger MPS, Schmidt DN (2015) Plio-Pleistocene climate sensitivity evaluated using high-resolution CO2 records. Nature 518. https://doi.org/10.1038/nature14145

Masson-Delmotte et al (2006) Past temperature reconstructions from deep ice cores. Relevance for future climate change. Clim Past 2:145–165 www.clim-past.net/2/145/2006/

Medina-Elizalde M, Lea DW (2005) The mid-Pleistocene transition in the tropical Pacific. Science 310:1009–1012

Menviel L, Timmermann A, Mouchet A, Timm O (2008) Meridional reorganizations of marine and terrestrial productivity during Heinrich events. Paleoceanography 23:PA1203. https://doi.org/10.1029/2007PA001445

Merkouriev S, DeMets C (2014) High-resolution Quaternary and Neogene reconstructions of Eurasia-North America plate motion. Geophys J Int. https://doi.org/10.1093/gji/ggu142

Moller T, Schulz H, Hamann Y, Dellwig O, Kucera M (2012) Sedimentology and geochemistry of an exceptionally preserved last interglacial sapropel S5 in the Levantine Basin (Mediterranean Sea). Mar Geol 291-294(2012):34–48. https://doi.org/10.1016/j.margeo.2011.10.011

Mosar J, Lewis G, Torsvik TH (2002) North Atlantic Sea-floor spreading rates: implications for the Tertiary development of inversion structures of the Norwegian–Greenland Sea. J Geol Soc London 159(2002):503–515

Mudelsee M, Raymo ME (2005) Slow dynamics of the Northern Hemisphere glaciation. Paleoceanography 20. https://doi.org/10.1029/2005PA001153

Ning S, Jia-Xin C, Königsson LK (1993) Late Cenozoic vegetational history and the Pliocene-Pleistocene boundary in the Yushe Basin, SE Shanxi, China. Grana 32(4-5):260–271. https://doi.org/10.1080/00173139309429990

Pagani M, Liu Z, LaRiviere J, Ravelo AC (2010) High Earth-system climate sensitivity determined from Pliocene carbon dioxide concentrations. Nat Geosci 3. https://doi.org/10.1038/NGEO724

Raymo ME (1994) The initiation of northern hemisphere glaciation. Annu Rev Earth Planet Sci 22:353–383

Raymo ME (1998) Glacial puzzles. Science 281(5382):1467–1468

Raymo ME, Lisiecki LE, Nisancioglu KH (2006) Plio-Pleistocene ice volume, Antarctic climate, and the global $\delta^{18}O$ record. Science 313:492–495

Raymo ME, Ruddiman WF (1992) Tectonic forcing of late Cenozoic climate. Nature 359:117–122

Rial JA, Pielke RA Sr, Beniston M, Claussen M, Canadell J, Cox P, Held H, de Noblet-Ducoudré N, Prinn R, Reynolds JF, Salas JD (2004) Nonlinearities, feedbacks and critical thresholds within the Earth's climate system. Clim Change 65(1–2):11–38

Rowley DB (2002) Rate of plate creation and destruction 180 Myr to present. Geol Soc Am Bull 114:927–933

Royer DL (2006) CO_2-forced climate thresholds during the Phanerozoic. Geochim Cosmochim Acta 70(2006):5665–5675

Rubincam DP (1993) The obliquity of Mars and climate friction. J Geophys Res 98:10827–10832

Rubincam DP (1995) Has climate changed the Earth's tilt ? Paleoceanography 10(3):365–372

Ruggieri E, Herbert T, Lawrence KT, Lawrence CE (2009) Change point method for detecting regime shifts in paleoclimatic time series. Application to $\delta^{18}O$ time series of the Plio-Pleistocene. Paleoceanography 24:PA1204. https://doi.org/10.1029/2007PA001568

Schneider R, Schmitt J, Köhler P, Joos F, Fischer H (2013) A reconstruction of atmospheric carbon dioxide and its stable carbon isotopic composition from the penultimate glacial maximum to the last glacial inception. Clim Past 9:2507–2523. https://doi.org/10.5194/cp-9-2507-2013

Schrag DP, Berner RA, Hoffman PF, Halverson GP (2002) On the initiation of a snowball Earth. Geochem Geophys Geosyst 3(6). https://doi.org/10.1029/2001GC000219

Seki O, Foster GL, Schmidt DN, Mackensen A, Kawamura K, Pancost RD (2010) Alkenone and boron-based Pliocene pCO_2 records. Earth Planet Sci Lett 292(2010):201–211. https://doi.org/10.1016/j.epsl.2010.01.037

Shackleton NJ (2000) The 100,000-year ice-age cycle identified and found to lag temperature, carbon dioxide, and orbital eccentricity. Science 289:1897–1902

Shackleton NJ, Opdyke ND (1977) Oxygen isotope and paleomagnetic evidence for early northern hemisphere glaciation. Nature 270:216–219

Stap LB, de Boer B, Ziegler M, Bintanja R, Lourens LJ, van de Wal RSW (2016) CO_2 over the past 5 million years: continuous simulation and new $\delta^{11}B$-based proxy data. Earth Planet Sci Lett 439(2016):1–10. https://doi.org/10.1016/j.epsl.2016.01.022

Stap LB, van de Wal RSW, de Boer B, Bintanja R, Lourens LJ (2014) Interaction of ice sheets and climate during the past 800 000 years. Clim Past 10:2135–2152. https://doi.org/10.5194/cp-10-2135-2014

Sun J, Huang X (2006) Half-precessional cycles recorded in Chinese loess: response to low-latitude insolation forcing during the last interglaciation. Quat Sci Rev 25(9–10):1065–1072. https://doi.org/10.1016/j.quascirev.2005.08.004

Svensen H, Planke S, Malthe-Sørenssen A, Jamtveit B, Myklebust R, Eidem TR, Rey SS (2004) Release of methane from a volcanic basin as a mechanism for initial Eocene global warming. Nature 429:542–545

Tachikawa K, Timmermann A, Vidal L, Sonzogni C, Timm OE (2014) CO_2 radiative forcing and intertropical convergence zone influences on western Pacific warm pool climate over the past 400 ka. Quat Sci Rev 86(2014):24–34. https://doi.org/10.1016/j.quascirev.2013.12.018

Tarnocai C, Canadell JG, Schuur EAG, Kuhry P, Mazhitova G, Zimov S (2009) Soil organic carbon pools in the northern circumpolar permafrost region. Global Biogeochem Cycles 23:GB2023. https://doi.org/10.1029/2008GB003327

Tziperman E, Raymo ME, Huybers PJ, Wunsch C (2006) Consequences of pacing the Pleistocene 100 kyr ice ages by nonlinear phase locking to Milankovitch forcing. Paleoceanography 21(PA4206):1–11. https://doi.org/10.1029/2005PA001241

Van de Wal RSW, de Boer B, Lourens LJ, Kohler P, Bintanja R (2011) Reconstruction of a continuous high-resolution CO_2 record over the past 20 million years. Clim Past 7:1459–1469. www.clim-past.net/7/1459/2011/. https://doi.org/10.5194/cp-7-1459-2011

Van Der Meer D.G., Zeebe R.E., van Hinsbergen D.J.J., Sluijs A., Spakman W. & Torsvik T.H. (2014) - Plate tectonic controls on atmospheric CO_2 levels since the Triassic. PNAS Early Edition, www.pnas.org/cgi/doi/10.1073/pnas.1315657111

Vautard R, Ghil M (1989) Singular spectrum analysis in nonlinear dynamics, with applications to paleoclimatic time series. Physica D 35(1989):395–424 North-Holland, Amsterdam

Walker JCG, Hays PB (1981) A negative feedback mechanism for the long-term stabilization of Earth's surface temperature. J Geophys Res 86(C10):9776–9782

Westerhold T, Röhl U, Frederichs T, Agnini C, Raffi I, Zachos JC, Roy H, Wilkens RH (2017) Astronomical calibration of the Ypresian timescale: implications for seafloor spreading rates and the chaotic behavior of the solar system? Clim Past 13:1129–1152 https://doi.org/10.5194/cp-13-1129-2017

Williams DM, Kasting JF, Frakes LA (1998) Low-latitude glaciations and rapid changes in the Earth's obliquity explained by obliquity–oblateness feedback. Nature 396:453–455

Wunsch C (2004) Quantitative estimate of the Milankovitch-forced contribution to observed Quaternary climate change. Quat Sci Rev 23(2004):1001–1012. https://doi.org/10.1016/j.quascirev.2004.02.014

Zachos JC, Dickens GR, Zeebe RE (2008) An early Cenozoic perspective on greenhouse warming and carbon-cycle dynamics. NATURE, Vol. 451,17 January 2008. https://doi.org/10.1038/nature06588

Zachos JC, Pagani M, Sloan L, Thomas E, Billups K (2001) Trends, rhythms, and aberrations in global climate 65 Myr to present. Science 292, pp.686-693.

Zagwijn WH (1974) The Pliocene--Pleistocene boundary in western and southern Europe. BOREAS. Vol. 3:75–97

Zhang Y.G., Pagani M., Liu Z., Bohaty S.M. & DeConto R. (2013) - A 40-million-year history of atmospheric CO_2. PHIL. TRANS. R. SOC. A, 371: 20130096. https://doi.org/10.1098/rsta.2013.0096